EPJ Nuclear Sci. Technol. **5**, 11 (2019)

https://doi.org/10.1051/epjn/2019030

EPJ Nuclear Sciences & Technologies

Available online at:
https://www.epj-n.org

Regular Article

Modelling of fine fragmentation and fission gas release of UO_2 fuel in accident conditions

Lars O. Jernkvist[*]

Quantum Technologies AB, Uppsala Science Park, 75183 Uppsala, Sweden

Received: 18 June 2019 / Received in final form: 23 August 2019 / Accepted: 6 September 2019

Abstract. In reactor accidents that involve rapid overheating of oxide fuel, overpressurization of gas-filled bubbles and pores may lead to rupture of these cavities, fine fragmentation of the fuel material, and burst-type release of the cavity gas. Analytical rupture criteria for various types of cavities exist, but application of these criteria requires that microstructural characteristics of the fuel, such as cavity size, shape and number density, are known together with the gas content of the cavities. In this paper, we integrate rupture criteria for two kinds of cavities with models that calculate the aforementioned parameters in UO_2 LWR fuel for a given operating history. The models are intended for implementation in engineering type computer programs for thermal-mechanical analyses of LWR fuel rods. Here, they have been implemented in the FRAPCON and FRAPTRAN programs and validated against experiments that simulate LOCA and RIA conditions. The capabilities and shortcomings of the proposed models are discussed in light of selected results from this validation. Calculated results suggest that the extent of fuel fragmentation and transient fission gas release depends strongly on the pre-accident fuel microstructure and fission gas distribution, but also on rapid changes in the external pressure exerted on the fuel pellets during the accident.

1 Introduction

There are several mechanisms for cracking and fragmentation of oxide (UO_2 or $(U,Pu)O_2$) nuclear fuel pellets. Tensile thermo-elastic stresses are induced at the pellet periphery by the steep radial temperature gradient that arises in the low thermal conductivity material under normal reactor operation. These stresses cause radial cracks to form at a linear heat generation rate (LHGR) of $5{-}6\,\mathrm{kWm}^{-1}$. The cracking proceeds as the power is increased, and the strength of the temperature gradient caused by the applied power dictates how many fragments need be created to keep the tensile stresses below the fracture threshold for the material [1,2]. The number of radial cracks (or fragments) increases initially almost linearly with increasing LHGR, but the tendency for further cracking declines at an LHGR above $40{-}45\ \mathrm{kWm}^{-1}$, as a result of increased material plasticity at high temperature. The number of cracks is also observed to increase slightly with fuel operating time or burnup [3].

The observed number of cracks rarely exceeds 15 in solid UO_2 fuel pellets that have experienced normal operating conditions during their lifetime [2–4], which means that fuel pellet fragments formed by thermal stresses under normal operating conditions are generally larger than 2 mm. However, finer fragments may form in accident conditions that involve very steep temperature gradients in the fuel material. This is the case, for example, in a reactivity initiated accident (RIA), where the fuel pellets are heated to high temperature within tens of milliseconds [5]. The steep temperature gradient that arises at the pellet periphery during the thermal shock induces a dense pattern of fine radial cracks close to the pellet surface [6,7]. Similar crack patterns may also form at the end of a loss-of-coolant accident (LOCA), when the fuel is re-wetted (quenched) from high temperature [8]. The fragments formed by thermally induced stresses during these accident conditions are typically 0.1–0.5 mm in size, and they are found predominantly at the pellet surface.

Even finer fuel fragments may form under certain accident conditions by overpressurization of gas-filled bubbles and pores in the solid. This fragmentation mechanism, which is the topic of this paper, is fundamentally different from the aforementioned processes that are related to thermally induced stresses. It has the potential to pulverize the material and create fragments down to the size of individual grains, i.e. $\approx 10\,\mu\mathrm{m}$ for typical UO_2 fuel. The first observations of fission gas induced fragmentation of oxide nuclear fuel were made in the early 1970s, more specifically in transient heating tests of liquid metal

---

[*] e-mail: loje@quantumtech.se

fast breeder reactor (LMFBR) UO_2 and $(Pu,U)O_2$ fuel. The new phenomenon was initially called "fuel dust cloud breakup", alluding to the rapid and energetic disruption into fine fragments that was observed in out-of-reactor tests [9,10]. Today, the gas induced fuel fragmentation is often referred to as fuel pulverization, powdering or fine fragmentation, in order to discriminate it from the larger-scale cracking and fragmentation that result from thermally induced stresses in the solid. The phenomenon was immediately identified as a safety issue, and it received much attention in research on LMFBR fuel safety during the 1970s and 1980s: summaries of this work can be found in [11–13]. Computational models, in the form of grain boundary fracture criteria, were formulated along with these early tests on LMFBR fuel [14–17]. The criteria were implemented in computer programs for analyses of LMFBR fuel, which are no longer in use.

Early on, it was clear that the gas induced fracture mechanism occurred only at high heating rate, typically in the range 10^2–10^5 Ks^{-1}, and/or at high temperature, and that the fuel had to be "sensitized" by accumulating a sufficient amount of fission gas in grain boundary bubbles, which required a certain fuel burnup. The heating rate dependence was interpreted as a competition between instant pressure relief of the bubbles by grain boundary fracture and time-dependent mechanisms for pressure relaxation, such as bubble growth or venting of the overpressurized bubbles through tortuous flow paths [13,17]: if the heating is fast enough, the thermally induced increase in bubble pressure will outrun the pressure relaxation by these time dependent mechanisms, and if the material is heated to a sufficiently high temperature, the overpressure will eventually break the grain boundaries. From this conception, it follows that grain boundary fracture will occur in parallel with time dependent relaxation mechanisms for certain heating rates. This has been corroborated experimentally [13,18].

Fission gas induced fuel fragmentation received renewed interest in the 1990s, when experimental programs on the behaviour of high burnup light water reactor (LWR) fuel under RIA conditions were conducted worldwide in the aftermath of the Chernobyl accident [5]. UO_2 and $(U,Pu)O_2$ fuel rodlets with burnups exceeding 40 MWd(kgHM)^{-1} were pulse irradiated in dedicated research reactors, such that fuel heating rates up to 10^5 Ks^{-1} were achieved. As a result of the rapid heating in combination with high fuel burnup, the fuel material broke up in much the same way as was observed for LMFBR fuel in the 1970s, and the fragmentation was accompanied with extensive fission gas release [19,20]. Prompted by these findings, a few new fracture criteria for the grain boundaries were developed in the 1990s, with the aim to model transient fission gas release (TFGR) in RIA conditions [21,22].

A decade later, out-of-reactor fission gas release experiments [23,24] and integral-type LOCA simulation tests [25,26] on UO_2 LWR fuel showed that fission gas induced fuel fragmentation may come into play also under fairly slow heating to moderate temperature, provided that the fuel burnup is sufficiently high. More precisely, the tests suggest that a fuel pellet average burnup above 60–65 MWd(kgU)^{-1} is needed for the gas induced fragmentation to occur at heating rates and temperatures that are expected in scenarios for LWR LOCA. Since these burnups are reached in many modern fuel designs, fission gas induced fuel fragmentation and its possible consequences to the fuel behaviour under LOCA have lately been in focus for much research. An example is the third phase of the Studsvik Cladding Integrity Project (SCIP-III), conducted under the auspices of the OECD Nuclear Energy Agency [27]. Part of this international research project aims to determine parametric thresholds for fuel fine fragmentation in LOCA conditions by experiments on high burnup LWR fuel. Empirical thresholds of this kind, focussing on fuel local burnup and temperature, were proposed in 2014, based on an assessment of the data available at that time [28,29]. This assessment showed that the susceptibility to fuel pulverization was highly correlated to the formation of a high burnup structure (HBS) at the pellet rim, but that pulverization occurred also outside the restructured rim zone. The pulverization was generally related to a high local population of overpressurized gas bubbles in the fuel material, and not to the HBS formation per se. In addition, the assessment revealed that the degree of pulverization, and hence, the resulting fragment size, depended on the heating rate and the temperature reached during the transient: the higher the heating rate and peak temperature, the smaller the fragments. It was also found that the gas induced fuel fragmentation and its associated TFGR can be substantially reduced by the imposition of a hydrostatic pressure on the fuel material. A pressure of about 50 MPa was reported to suppress pulverization, which means that mechanical constraint from pellet-cladding interaction may limit pulverization and transient fission gas release in high burnup LWR fuel rods [28,29]. This conclusion has been confirmed by out-of-reactor heating tests, in which pulverization and TFGR were measured for UO_2 fuel rodlets that did or did not experience cladding ballooning and burst during the test [30,31]. The results indicate that pulverization and fission gas release is enhanced in rods that experience cladding ballooning, and further enhanced in rods that also experience cladding burst with a sudden drop in internal gas pressure [30,31]. It is believed that the sudden loss of fuel mechanical constraint that the cladding ballooning and burst brings about helps trigger the fine fragmentation.

There are several safety issues related to fission gas induced fuel fragmentation under typical design basis accident conditions, such as RIAs and LOCAs. Firstly, the TFGR associated with the fragmentation may significantly increase the fuel rod internal gas pressure, which may contribute to ballooning and burst of the cladding tubes. This is a potential failure mode for the fuel rods in both RIAs [5] and LOCAs [32]. Secondly, the formation of fine fuel fragments may increase the amount of fuel material that is ejected from failed rods into the coolant. This is partly a geometrical effect: small fuel fragments are more likely to relocate axially within the cladding tube and to escape through the cladding breach, entrained in the stream of outflowing gas. The increased amount of ejected fragments, and the increased release of gaseous fission products that the fine fragmentation brings about, will worsen the radiological consequences of an accident. There is also some concern about the long term coolability and the risk for criticality of the fuel that is dispersed into the coolant [33]. Thirdly, the hot fuel fragments ejected from failed fuel rods will interact with the coolant. Fuel coolant interaction (FCI) is a mechanism that may potentially lead to core damage in worst-case scenarios for LWR RIAs [5]. Fine fragmentation of the fuel will aggravate the FCI, since the energy conversion ratio, i.e. the ratio of the mechanical energy generated by coolant vaporization to the thermal energy in the dispersed fuel, is inversely proportional to the fuel fragment size [5].

With regard to mathematical modelling and computational analyses of fission gas induced fuel fragmentation and transient fission gas release, applications have with some exception [34] hitherto been on reactivity initiated accident conditions. For example, the models and analyses in [35–38] are fairly recent applications to oxide LWR fuel in RIA conditions. Various analytical criteria have been used in the models to determine whether fine fragmentation will occur under given conditions, but all the criteria are based on the assumption that there is a critical overpressure for bubbles and pores, at which the surrounding fuel material will break in a brittle manner. The overpressure, or excess pressure P_{ex}, is in most criteria calculated from

$$\begin{aligned} P_{ex} &= P_g - P_{eq} = P_g - P_h - P_s \\ &= P_g + \mathrm{trace}(\boldsymbol{\sigma})/3 - \gamma\left(\frac{1}{R_1} + \frac{1}{R_2}\right), \end{aligned} \tag{1}$$

where P_g is the current gas pressure and $P_{eq} = P_h + P_s$ is the equilibrium pressure in the cavity. Here, $P_h = -\mathrm{trace}(\boldsymbol{\sigma})/3$ is the hydrostatic pressure in the fuel material with a three-dimensional stress state given by the Cauchy stress tensor $\boldsymbol{\sigma}$, and P_s is the capillary pressure in the considered cavity. The latter is given by the Young-Laplace equation, where R_1 and R_2 are the principal radii of curvature for the cavity and γ is the fuel/gas specific surface energy.

Calculation of the cavity excess pressure thus requires determination of both the gas pressure and the equilibrium pressure. This is not an easy task from a modelling point of view: the gas pressure calculation requires an equation of state that is applicable to high pressures and that the input to this equation, namely the cavity volume and gas inventory (molecular density and composition of gaseous fission products) are accurately calculated together with the gas temperature. Prevalent computational tools for thermal-mechanical analyses of nuclear fuel do not generally model the fuel microstructure evolution and the fission gas distribution at this level of detail [39]. This is particularly true for the evolution of the high burnup structure. Likewise, for calculating the gas equilibrium pressure, information is needed on the fuel stress state and the geometry (size and shape) of the gas-filled cavities. The local stress state is difficult to calculate for oxide fuel under reactor operation, since it is affected by pellet-cladding mechanical interaction (PCMI) and fuel cracks induced by temperature gradients and non-uniform swelling.

In this paper, computational models are presented, by which the aforementioned data are estimated and used as input to rupture criteria for grain boundary bubbles and HBS pores. The objective is to formulate a set of models that can be used for calculating the extent of fuel fragmentation and transient fission gas release under design basis LOCA and RIA. The presented models calculate the distribution of gaseous fission products and the evolution of microstructure in UO_2 fuel with regard to intergranular bubbles and HBS pores under long-term steady-state reactor operation and transients. The models are fairly simple and intended for implementation in engineering type computer programs for thermal-mechanical analyses of LWR fuel rods. We have implemented and validated the models in the FRAPCON-4.0P1 and FRAPTRAN-1.5 programs [40,41], which are good examples of the intended category of host codes. Over the years, our in-house version of FRAPTRAN-1.5 has been extended and improved with respect to modelling of fuel rod thermal-mechanical behaviour under LOCA conditions. Previous extensions include models for cladding high temperature deformation, oxidation and burst, as well as models for axial relocation of fuel fragments and its effects on the fuel rod heat load and failure processes in LOCA conditions [42]. The set of models presented in the following is the latest improvement of the program.

The paper is organized as follows: The models are presented and discussed in light of open literature experimental data in Section 2. Results from validation of the models against selected experiments on fission-gas induced fragmentation of UO_2 fuel under simulated LOCA and RIA conditions are presented in Section 3, with the intention to illustrate the modelling approach. Conclusions of the work are finally given in Section 4.

2 Considered phenomena and applied models

In our model, fine fragmentation of the fuel is assumed to occur by overpressurization of two types of cavities: micron-sized spherical pores in the HBS at the pellet rim, and/or lenticular sub-micron bubbles on grain faces (planar boundaries where two grains meet) of non-restructured fuel material in the interior of the pellet. The considered grain face geometry is shown in Figure 1. For the lenticular grain face bubbles, the surface energy γ in equation (1) is actually an effective quantity, given by $\gamma_e = \gamma_{fs} - \gamma_{gb}/2$, where γ_{fs} is the true fuel/gas specific surface energy and γ_{gb} is the grain boundary energy [17]. These energies are related through $\gamma_{gb} = 2\gamma_{fs}\cos\theta$ [43], which means that $\gamma_e = \gamma_{fs}(1 - \cos\theta)$. This apparent reduction in surface energy for lenticular grain face bubbles has been observed experimentally [44].

In each spatial integration point, the local population of pores or bubbles is represented by an *average* size pore or bubble, meaning that the size distributions of the cavities

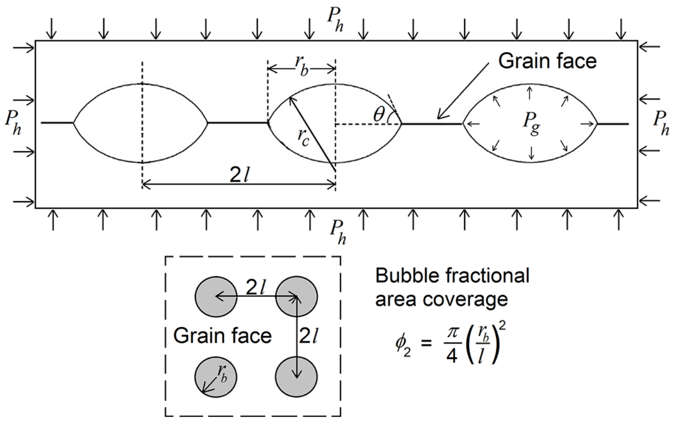

Fig. 1. A periodic array of identical lenticular bubbles along a planar grain face, as considered in the model. r_b: projected bubble radius, r_c: radius of curvature, $2l$: bubble spacing, θ: semi-dihedral angle.

are not explicitly considered. Only the space-time variation of the average properties are calculated. Empirical models are used for calculating the formation and evolution of HBS pores, whereas a combination of analytical and empirical models is used for the grain face bubbles. The models applied for calculating the average size and number density of the two types of cavities are closely linked to the models for fission gas production, transport and release. In the following, we describe the submodels applied for each phenomenon and how the submodels interact.

2.1 Fission gas production, transport and distribution

The key equations for fission gas production, transport and distribution applied in our model originate from the seminal work of Speight [45], and they are solved numerically by the method proposed by Forsberg and Massih [46] with later improvements by Hermansson and Massih [47]. A recent review of the subject can be found elsewhere [48].

2.1.1 Intragranular gas diffusion and trapping

Intragranular gas diffusion is treated by an equivalent sphere model. This is a widely used modelling approach, in which the polycrystalline fuel material is considered as a collection of spherical grains of uniform size, characterized by a single equivalent radius, r_g. Following the work of Speight [45], we assume that the spherical grains contain traps for the diffusing gas atoms in the form of intragranular bubbles. The total concentration of gas in the grain, C_g, can be partitioned into dissolved (mobile) gas, C_d, and trapped gas, C_t. Trapping of the dissolved gas into the intragranular bubbles takes place at a rate ν_t and re-solution of trapped gas into the fuel matrix occurs at a rate ν_d. Fission gas is produced at a rate β per unit volume of the fuel matrix. All these properties depend on space and time, but they are assumed to be uniform within individual grains. For a particular position in the fuel pellet column, the governing equations for diffusion within the spherical grain read

$$\frac{\partial C_d(r,t)}{\partial t} = D_l \nabla^2 C_d(r,t) \\ -\nu_t C_d(r,t) + \nu_d C_t(r,t) + \beta(t), \qquad (2)$$

$$\frac{\partial C_t(r,t)}{\partial t} = \nu_t C_d(r,t) - \nu_d C_t(r,t), \qquad (3)$$

where ∇^2 is the Laplacian operator and D_l is the diffusivity of dissolved gas atoms in the UO_2 lattice. Equations (2) and (3) do not include fission gas atoms that are lost due to recoil and knockout processes. These are athermal release processes, considered through the boundary conditions for the above equations; see Section 2.1.3. Assuming that trapping and re-solution of gas in the intragranular bubbles is fast in comparison with the characteristic diffusion time $r_g^2/6D_l$, the traps can be considered as saturated with gas at a concentration of $C_t = C_d\nu_t/\nu_d$. By using this approximation and adding equations (2) and (3), we arrive at the following expression for the total concentration of intragranular gas, $C_g = C_d + C_t$:

$$\frac{\partial C_g(r,t)}{\partial t} = D_l \nabla^2 \left(\frac{C_g(r,t)\nu_d}{\nu_d + \nu_t} \right) + \beta(t). \qquad (4)$$

Finally, since the ratio $\nu_d/(\nu_d + \nu_t)$ is assumed to be independent of the radial position within the spherical grain, equation (4) simplifies to

$$\frac{\partial C_g(r,t)}{\partial t} = D_{\text{eff}} \nabla^2 C_g(r,t) + \beta(t), \qquad (5)$$

where $D_{\text{eff}} = D_l\Omega_g$ is an effective diffusivity that accounts for gas trapping in intragranular bubbles through the reduction factor Ω_g. For steady-state equilibrium conditions, it follows from equation (4) that the trapping factor $\Omega_g = \nu_d/(\nu_d + \nu_t)$. For general time-varying conditions, the trapping factor is in our model calculated through

$$\frac{\partial \Omega_g(r,t)}{\partial t} = \frac{\Omega_{g\infty} - \Omega_g}{\tau_g}, \qquad (6)$$

where $\Omega_{g\infty} = \nu_d/(\nu_d + \nu_t)$ is the equilibrium value and the time constant τ_g is a model parameter; see Table 1. The boundary conditions for equation (5) are defined in Section 2.1.2.

The gas atom lattice diffusivity D_l is in our model calculated through a three-term correlation proposed by Turnbull et al. [49,50], while the trapping and resolution rates for gas atoms interacting with intragranular bubbles are calculated through [51,52]

$$\nu_t = 4\pi D_l r_{bi} n_{bi}, \qquad (7)$$

$$\nu_d = 3.03\pi\varphi l_f (r_{bi} + \delta_f)^2, \qquad (8)$$

where r_{bi} and n_{bi} are the mean radius and number density of intragranular bubbles, l_f and δ_f are the typical track length and range of influence for a fission fragment, and φ is the fission rate density. The expressions used for these parameters are given in Table 1.

Table 1. Properties assumed for fission gas production, diffusion and distribution. N_A is the Avogadro number, T denotes temperature in kelvin and φ is the local fission rate density in fissions $(\mathrm{m}^3\mathrm{s})^{-1}$. The coefficient used for the athermal part of D_l is an average of the values proposed in [50,53].

Property/parameter			Unit	Source
β	$=$	$0.31\varphi/N_A$	$[\mathrm{mol}/(\mathrm{m}^3\mathrm{s})]$	[40]
B_{gb}	$=$	$1.44\times10^{-8}\beta$	[m/s]	This work
D_l	$=$	$7.60\times10^{-10}e^{-35247/T}$		
	$+$	$5.64\times10^{-25}\sqrt{\varphi}e^{-13800/T}$	$[\mathrm{m}^2/\mathrm{s}]$	[49,50,53]
	$+$	$1.00\times10^{-39}\varphi$		
τ_g	$=$	7.2×10^{4}	[s]	This work
r_{bi}	$=$	$1.453\times10^{-10}e^{T/978}$	[m]	[54]
n_{bi}	$=$	$1.52\times10^{27}/T-3.3\times10^{23}$	$[\mathrm{m}^{-3}]$	[52,54]
l_f	$=$	6×10^{-6}	[m]	[55]
δ_f	$=$	1×10^{-9}	[m]	[52]
c_{rk}	$=$	1.4×10^{-4}	[(kgU)/(MWd)]	This work
r_g	$=$	4.2×10^{-6}	[m]	This work

2.1.2 Re-solution of gas from intergranular bubbles

The initial condition for the intragranular gas concentration is $C_g(r,0)=0$ and the boundary condition at the grain centre, $\partial C_g(0,t)/\partial r=0$, follows from spherical symmetry. The condition at the grain boundary $(r=r_g)$ caters for the presence of intergranular gas bubbles and resolution of gas from these bubbles back into the grain [45]. It is written

$$C_g(r_g,t)=\frac{B_{gb}(t)N_{gb}(t)}{D_{\mathrm{eff}}(t)}, \tag{9}$$

where N_{gb} is the surface concentration of gas atoms at the grain boundary and B_{gb} is a measure (in ms^{-1}) of the resolution rate of gas atoms from the grain boundary back into the grain. Equation (9) defines an *effective* gas concentration at the grain boundary, controlled by B_{gb}, which represents gas atoms in intergranular bubbles that are knocked back into the grain by collision with fission fragments. In reality, these gas atoms reach a finite distance into the grain. Since the resolution is caused by fission spikes, B_{gb} is assumed to be proportional to the fission rate; see Table 1.

2.1.3 Fission gas release

Some fission gas atoms located close to free surfaces of pellet fragments escape to the rod free volume by direct recoil and knockout [56,57]. These are athermal (temperature independent) processes, and in our model, we calculate the amount of local athermal gas release per unit volume of fuel by recoil and knockout through

$$F_{rk}(t)=c_{rk}\int_0^t E(\tau)\beta(\tau)d\tau, \tag{10}$$

where E is the local fuel burnup and c_{rk} is a constant model parameter; see Table 1.

Gas in grain boundary bubbles may be vented and released to the rod free volume by formation of interconnected flowpaths or by complete rupture of the grain boundaries. In these cases, restrictions apply to the grain boundary surface concentration of gas N_{gb}, see Section 2.2.2, and the amount of local fission gas release from the grain boundaries per unit volume of fuel can be written

$$\begin{aligned}F_{gb}(t)=\int_0^t\beta(\tau)d\tau-F_{rk}(t)-\frac{3N_{gb}(t)}{2r_g}\\-\frac{3}{r_g^3}\int_0^{r_g}r^2C_g(r,t)dr,\end{aligned} \tag{11}$$

where the right-hand-side terms represent produced gas, athermally released gas, intergranular gas and intragranular gas. Equation (11) provides the relationship between $N_{gb}(t)$ and $C_g(r,t)$ that is needed in case N_{gb} is not directly given by the criteria for grain boundary fission gas release in Section 2.2.2. Together with equation (9), it defines the partitioning of intragranular versus intergranular retained gas. Equations (5)–(11), combined with the criteria for grain boundary fission gas release in Section 2.2.2, are solved at each spatial integration point for time-varying conditions by use of an efficient numerical method [46,47]. The equivalent grain radius, r_g, is assumed to be invariant with time, but may vary in space. It is a *representative* value, adapted to the grain size distribution in the considered material.

If the fuel reaches a sufficiently high burnup that local restructuring of the material occurs, gas release controlled by intragranular diffusion to grain faces is no longer considered in our model, since other fission gas release mechanisms come into play. The models applied for these mechanisms are described in Section 2.3.

2.2 Evolution of grain face bubbles

2.2.1 Bubble nucleation, growth and coalescence

The evolution of fission gas bubbles on grain faces has been experimentally studied for UO_2 fuel in the past [58–62]. These studies show that small lenticular bubbles nucleate on the grain faces already at low fuel burnup. Metallic precipitates at the grain faces evidently act as nucleation sites for the bubbles and hinder their movement

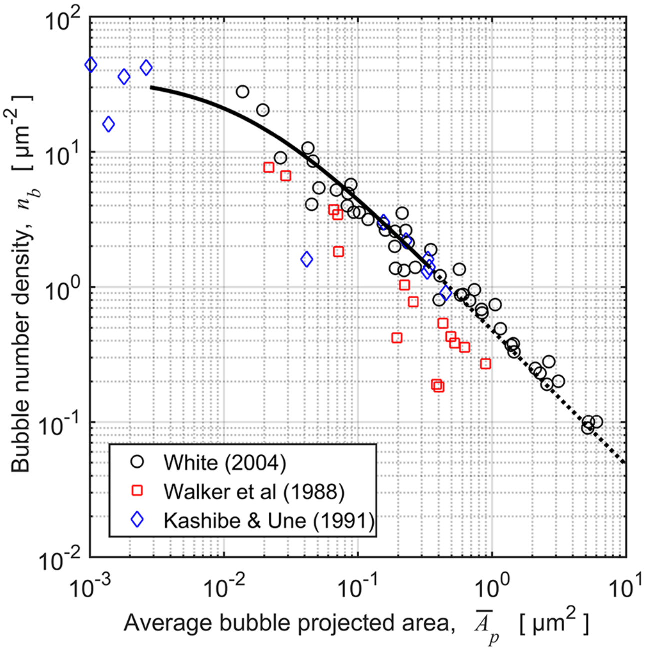

Fig. 2. Number density of grain face bubbles versus the average projected area of the bubbles, observed in UO_2 fuel with pellet average burnups between 9 and 33 MWd(kgU)$^{-1}$ by White [62], Walker et al. [59] and Kashibe and Une [61]. The solid line is a plot of equation (12) over its range of application in the model. The dashed line represents the saturated grain face condition $\phi_2 = n_b\bar{A}_p = 0.48$.

during subsequent growth [58,59]. At first, the bubbles grow without much change in their number density, but with further growth, the bubble density decreases as the bubble size increases. This is illustrated by Figure 2, which summarizes reported data on the size-density relation for grain face bubbles in UO_2 fuel. Although differences exist between the data sets, mainly because of differences in fuel operating history and experimental methods, the decreasing trend for the number density is evident. The reduction in bubble density is partly attributed to Ostwald ripening [59], but another reason for the coarsening is that the lenticular bubbles start to coalesce when their fractional coverage of the grain face reaches about 0.18 [62]. The coalescence leads to the occurrence of elongated (vermicular) and multi-lobal bubbles. An extensive data set on observed size and shape evolution of grain face bubbles in ramp tested UO_2 fuel is available through the International Fuel Performance Experiments (IFPE) database [63] and the data are summarized in [62]. Supported by these data, White [62] derived a simple relationship between the projected area, A_p, and the number density, n_b of the grain face bubbles by considering the coalescence of identical bubbles as a reaction limited process. The relationship reads

$$n_b(A_p) = n_b^o\left(1 + 2n_b^o(A_p - A_p^o)\right)^{-1}, \qquad (12)$$

where A_p^o and n_b^o are the initial projected area and number density of the nucleated bubbles. Equation (12) is plotted in Figure 2 for $n_b^o = 3.0 \times 10^{13}$ m^{-2} and $A_p^o = 2.83 \times 10^{-15}$ m^2, corresponding to a lenticular bubble nucleus with a projected radius of 30 nm. The equation fits the data by Kashibe and Une [61] and White [62] fairly well, notwithstanding that it is an approximation, derived for a collection of bubbles with identical size and assuming that coalesced bubbles retain the same projected area as the parent bubbles. Various modifications and improvements to equation (12) have been suggested, in which the volume rather than the projected area of coalescing bubbles is retained [64,65]. These alternative approaches have been tested in our model, but since they were found not to improve the model's capacity to reproduce experimental data, we make use of equation (12) in its original form for calculating the reduction in bubble number density as the bubbles grow and finally saturate the grain faces.

The growth of intergranular voids has been theoretically studied in different contexts in the past, see e.g. [66,67]. A model that has been widely used for the growth of grain face bubbles in UO_2 is due to Speight and Beeré [68], who considered a grain face bubble with circular projection that grows by diffusion of vacancies along the grain face to the bubble. By considering a circular diffusion cell, in which the bubble covers a fraction ϕ_2 of the cell area, they found the following expression for the rate of change of the bubble volume V_b

$$\frac{dV_b}{dt} = \frac{2\pi\Omega\omega D_{gb}^v}{k_B T L(\phi_2)} P_{ex}. \qquad (13)$$

Here, Ω is the atomic volume of the solid, in our case the volume of the uranium atom, D_{gb}^v is the grain boundary vacancy self diffusion coefficient, ω the thickness of the diffusion layer along the grain boundary, k_B Boltzmann's constant and T the absolute temperature; see Table 2. P_{ex} is the gas bubble overpressure, defined by equation (1), which means that the balance between the bubble gas pressure, the hydrostatic pressure and the surface tension controls the growth or shrinkage of the bubble. $L(\phi_2)$ is a dimension-free function of the bubble fractional area coverage, ϕ_2, viz.

$$L(\phi_2) = \phi_2 - \frac{3 + \phi_2^2 + 2\ln(\phi_2)}{4}, \qquad (14)$$

which drops significantly as the bubbles grow and ϕ_2 increases. Hence, equation (13) is highly non-linear, since the fractional coverage and the bubble overpressure depend on the bubble volume. It is also strongly temperature dependent through the diffusion coefficient D_{gb}^v.

Over the years, the Speight-Beeré model has been applied for calculating gas-induced swelling of UO_2 fuel [35,62,65,70–73] and/or for calculating onset of fission gas release by growth and interconnection of grain face bubbles into continuous release paths for the gas [35,65,70,73–75]. In most of these applications, equation (13) has been used either with a fixed value for ϕ_2 in the calculations or under the assumption of a fixed number density, n_b, for the bubbles. Here, we take a more elaborate approach, similar to that by Pastore and co-workers

Table 2. Properties assumed for grain faces and grain face bubbles.

Property/parameter			Unit	Source
θ	=	47	[deg]	[43,69]
ω	=	5.0×10^{-10}	[m]	[70]
Ω	=	4.09×10^{-29}	[m^3]	[71]
n_b^o	=	3.0×10^{13}	[1/m^2]	[59,61,62]
A_p^o	=	2.83×10^{-15}	[m^2]	[59,61,62]
γ_{fs}	=	$0.89 - 1.4 \times 10^{-4}T$	[J/m^2]	[44]
$\mathscr{G}_{gb}$	=	4.0×10^{-3}	[J/m^2]	This work
υ	=	0.98	[–]	This work
D_{gb}^v	=	$6.90 \times 10^{-4} e^{-38770/T}$		
	+	$5.64 \times 10^{-25}\sqrt{\varphi} e^{-13800/T}$	[m^2/s]	This work, [70]
	+	$1.00 \times 10^{-39}\varphi$		

[65], in that we apply equation (13) with a time-varying fractional area coverage, ϕ_2, accounting for the evolution of bubble size and number density. In a population of grain face bubbles with different sizes and shapes, the fractional area coverage may be formally calculated through $\phi_2 = \int_0^\infty n_b(A_p)dA_p$, where A_p is the area of the bubble projected on the grain face and $n_b(A_p)$ is the number density (in m^{-2}) for this size class of bubbles. To ease the calculations, we do not explicitly account for the size distribution of the grain face bubbles, but use the *average* size for representing the population. This makes it possible to use equation (12) for estimating the bubble fractional coverage, viz.

$$\phi_2 = n_b(\bar{A}_p)\bar{A}_p, \tag{15}$$

where $\bar{A}_p$ is the *average* projected area of the bubbles and $n_b(\bar{A}_p)$ is White's relation in equation (12), applied to the average size bubble. The result is shown in Figure 3, together with measured data from the open literature. It is clear from Figure 3 that most of the experimental data for ϕ_2 fall below the curve defined by equations (12) and (15). This is not surprising, considering that we have approximated the fractional area coverage by equation (15) instead of considering the size distribution of the bubbles. Nevertheless, we believe that the approximation is good enough for our purposes, keeping in mind that the Speight-Beeré equation in itself is also an approximation. It is derived for bubbles of circular projection, and therefore strictly applicable to cases with $\phi_2 < 0.2$, where the grain face bubbles are well separated and predominantly of lenticular shape [62]. Nevertheless, we apply the Speight-Beeré equation to cases with ϕ_2 up to nearly 0.5, where the bubble aspect ratio (length/width) is typically 3–5 [62]. Under these conditions, bubbles grow by coalescence as well as by vacancy diffusion to individual bubbles. Another point to make about Figure 3 is that both the data and the model suggest that the fractional coverage saturates around 0.5. The saturation is due to the formation of continuous release paths for the grain boundary gas and relaxation of the bubble overpressure by gas release; see Section 2.2.2.

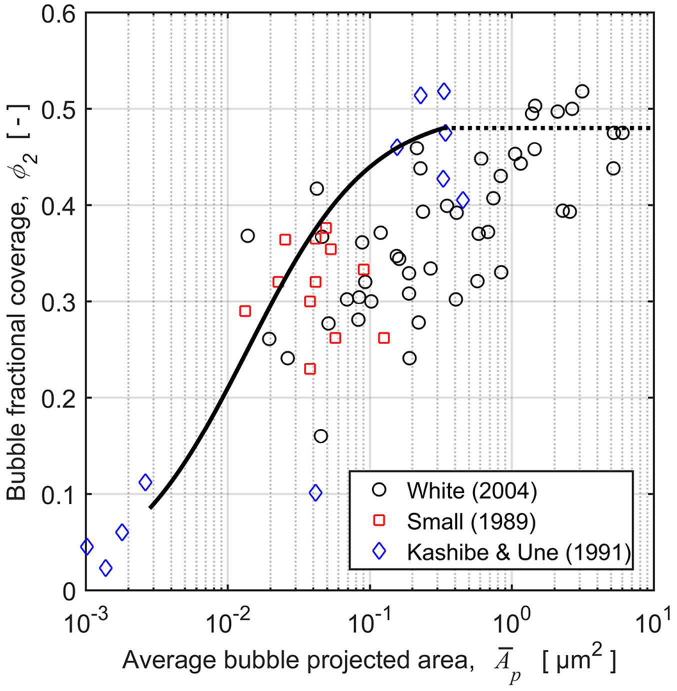

Fig. 3. Fraction of grain face area occupied by bubbles versus the average projected area of the bubbles, observed in UO$_2$ fuel with pellet average burnups between 9 and 28 MWd(kgU)$^{-1}$ by White [62], Small [60] and Kashibe and Une [61]. The solid line is a plot of equation (15), combined with $n_b(\bar{A}_p)$ from equation (12), and the dashed line represents the saturated grain face condition $\phi_2 = 0.48$.

In our computational model, we apply equations (12)–(15) to a lenticular grain face bubble as illustrated in Figure 1. The bubble represents the average size bubble in the population, meaning that the average projected area is $\bar{A}_p = \pi r_b^2$ and the average bubble volume is

$$\bar{V}_b = 4\pi\tilde{\eta}(\theta)r_b^3/3, \tag{16}$$

where $\tilde{\eta}(\theta) = (2 - 3\cos\theta + \cos^3\theta)/(2\sin^3\theta)$. The semi-dihedral angle θ is reported to be typically in the range 35–55° for grain face bubbles in UO$_2$ [43,69], leading to values for $\tilde{\eta}$ in the range of 0.25–0.43. Hence, the volume of a typical lenticular bubble is about one third of a spherical bubble with the same projected radius r_b. From a modelling point of view, θ (or $\tilde{\eta}$) can be seen as a tuning parameter that controls the ratio between bubble volume and projected area. With regard to our model, we expect θ and $\tilde{\eta}$ to be in the upper ends of the aforementioned intervals. The reason is that the modelled lenticular bubble will represent the overall grain face porosity, which includes vermicular bubbles with a comparatively large ratio between bubble volume and projected area.

Equations (12)–(15) are in our model applied to the average size lenticular grain face bubble, using the well known Carnahan-Starling equation of state for calculating the bubble gas pressure [76]. An efficient numerical integration of the resulting ordinary differential equation for V_b is essential for the overall performance of the host code, since this equation is repeatedly solved for the incremental change in V_b for each integration point in the discretized fuel pellet column. The differential equation becomes stiff at high temperature, and its integration requires non-standard methods; see Appendix A. Finally, it should be remarked that swelling/shrinkage of the fuel pellet material, induced by growth/shrinkage of grain face bubbles, is currently not considered in our model.

2.2.2 Bubble venting

Three mechanisms for venting and release of the gas in grain boundary bubbles are considered in our model: (1) venting by formation of a continuous network of growing bubbles at grain faces and grain edges; (2) venting by complete rupture of the grain boundaries as a result of rapid bubble overpressurization; (3) venting through a continuous network of grain face microcracks, formed by slow overpressurization of the grain face bubbles. Three different criteria are used for assessing whether any of these release modes is active locally at any given time. If so, the surface concentration of grain boundary gas, N_{gb} in equations (9) and (11), is assumed to approach a steady-state post-release value, $\tilde{N}^i_{gb}$, which is specific to the ith release mode. More precisely, we apply the first order differential equation

$$\frac{\partial N_{gb}}{\partial t} = \frac{1}{\tau_i}\left(\tilde{N}^i_{gb} - N_{gb}\right), \tag{17}$$

to calculate the change in N_{gb} for the release mode of interest. Hence, when the ith release mode is active, the grain boundary surface concentration tends to the steady-state post-release value $\tilde{N}^i_{gb}$ with a relaxation time τ_i. $\tilde{N}^i_{gb}$ is calculated from a postulated steady-state post-release value for the bubble gas pressure, $\tilde{P}^i_g$, through the Carnahan-Starling equation of state; see equations (A.9)–(A.11) in Appendix A. This gas pressure is defined in Table 3, together with the release criteria and relaxation times applied for the three release mechanisms. The modelling of these release mechanisms is discussed in further detail below. The value calculated for N_{gb} through equation (17) defines the grain boundary fission gas release through equations (5), (9) and (11).

(1) Bubble interconnection

If the grain face bubbles grow to such an extent that they connect with the grain edges, where three grains meet, a continuous network may form, through which part of the intergranular gas inventory can be vented to the rod free volume. Significant venting will occur only if the grain faces and grain edges connect over a larger volume of the material than just a few grains; computational analyses based on percolation theory suggest that more than about 60 % of the grain faces must be permeable for a long-range network to form and considerable fission gas release to occur [77,78].

Experimental data that provide information on bubble venting are available from the aforementioned study by White and co-workers [62,63]. Their ceramographic investigation of 427 grain faces from moderately irradiated UO_2 fuel, ramped to target fuel temperatures from 1500 to 2200 K, showed that less than 10 % of the examined grain faces had a fractional bubble coverage in excess of 0.5. The highest observed fractional coverage was just below 0.6 [62]. Similar results have been reported by Kashibe and Une [61]; see Figure 3. These results suggest that the gas pressure generally relaxes by bubble venting at a fractional coverage below 0.5, and exceptionally, at fractional coverages between 0.5 and 0.6.

Based on these data, we assume that a continuous network of interconnected grain face bubbles that allows venting of the gas in part of the bubbles forms when the grain face fractional area coverage of bubbles (ϕ_2) reaches 0.48. This threshold is significantly lower than the value of $\pi/4$ that was used in early models [70,79] and slightly lower than the value of 1/2 proposed more recently [65]. From equations (12) and (15), we may formulate the criterion for venting of grain face bubbles in terms of a threshold for the bubble projected radius instead of ϕ_2. Using, as before, $n^o_b = 3.0 \times 10^{13}$ m^{-2} and $A^o_p = 2.83 \times 10^{-15}$ m^2, the corresponding threshold for r_b is 325 nm. When this threshold for ϕ_2 or r_b is reached, we assume that grain boundary gas is released to such an extent that the bubble gas pressure approaches $P_h + P_s$, or in other words, that the bubble excess pressure P_{ex} tends to zero. It is clear from equation (13) that this condition implies that bubble growth will cease, and that ϕ_2 will not exceed 0.48. Hence, the experimentally observed saturation of the bubble grain face coverage at values close to 0.5 is captured by the model.

In reality, the gas pressure in a vented grain face bubble would equal the gas pressure in the pellet-cladding gap. However, in reality, there would also be a certain fraction of bubbles that remain unvented. Hence, setting the bubble gas pressure at time of venting equal to the gap gas pressure would pose a risk of overestimating the gas release. Also, by postulating the post-release gas pressure in the bubble to $P_h + P_s$, the concentration of gas retained in the partially vented grain face will depend on the fuel pellet stress state through the hydrostatic pressure P_h. This means that the model captures the observed effects

Table 3. Release criteria, steady-state post-release gas pressures in grain face bubbles, and relaxation times for the considered release mechanisms for grain boundary gas. P_g^{cr} is the critical bubble gas pressure for grain boundary rupture and υ is a constant model parameter less than unity; see below.

Mechanism (i) for grain boundary fission gas release	Criterion for gas release	Post-release gas pressure, $\tilde{P}_g^i$	Relaxation time [s], τ_i
(1) Bubble interconnection	$\phi_2 \geq 0.48$	$P_h + P_s$	2
(2) Grain boundary rupture	$P_g \geq P_g^{cr}$	P_g^{gap}	0
(3) Grain boundary microcracking	$\upsilon P_g^{cr} < P_g < P_g^{cr}$	υP_g^{cr}	2

of PCMI on fission gas release under power transients: the release is moderate under conditions of strong PCMI (high P_h), but may become significant and occur rapidly under power reductions, when the PCMI relaxes and P_h decreases [74,80].

In the once vented grain face bubbles, P_{ex} may turn negative as a result of either an increasing hydrostatic pressure on the fuel pellet, or a decreasing gas pressure in the bubble, e.g. by a temperature reduction. From equation (13), it is clear that this will cause shrinkage of the bubbles in our model. As the bubbles shrink, the fractional coverage ϕ_2 will decrease to a value below 0.48, i.e. the threshold for bubble interlinkage and venting. From a modelling point of view, this means that the once vented bubbles are re-closed, and that no further gas release will occur until the bubbles grow to such an extent that ϕ_2 again reaches 0.48.

(2) Grain boundary rupture

As mentioned in Section 1, there is substantial experimental evidence that grain boundaries in UO_2 and $(U,Pu)O_2$ nuclear fuel may rupture and turn the material into fine fragments as a consequence of severely overpressurized grain face bubbles. The fragmentation does not occur under steady-state operating conditions or mild transients, since the overpressure then has time to relax, either by growth and eventually venting of the bubbles or by gas slowly seeping out through microcracks formed in the grain boundaries. However, under accident conditions, the overpressure may increase at a rate that outruns these time-dependent relaxation mechanisms, either as a result of rapid fuel heating or by a sudden reduction of hydrostatic pressure in the fuel material. The first scenario is relevant for RIA, while the second scenario may occur as a result of cladding ballooning and burst under LOCA in high burnup fuel rods.

From a review of existing analytical thresholds for the overpressure in bubbles and pores, at which the surrounding fuel material is assumed to break [81], the rupture criterion by Chakraborty and co-workers [82] was identified as suitable for application to grain face bubbles. This criterion is based on linear elastic fracture mechanics and applied to a grain face containing an array of identical overpressurized lenticular bubbles with a semi-dihedral angle of 50°. According to Chakraborty and co-workers, the critical bubble gas pressure for rupture of the solid material along the grain face is [82]

$$\begin{aligned} P_g^{cr} &= P_h + P_s + \frac{K_{Ic}}{F_I(\phi_2)\sqrt{\pi r_b}} \\ &= P_h + P_s + \frac{1}{F_4(\phi_2)}\sqrt{\frac{\pi E_Y \mathscr{G}_{gb}}{(1-\nu^2) r_b}}, \end{aligned} \tag{18}$$

where $F_4(\phi_2) = \pi F_I(\phi_2) = \pi(0.568\phi_2^2 + 0.059\phi_2 + 0.5587)$ is a dimension-free function of the bubble fractional area coverage and K_{Ic} is the mode I linear elastic fracture toughness of the grain boundary. The latter is here expressed in terms of the grain boundary fracture energy $\mathscr{G}_{gb}$, the Young modulus E_Y and the Poisson ratio ν for the fuel material [83]. $\mathscr{G}_{gb}$ is a local material property that is virtually unknown, but it can be estimated by inverse modelling, i.e. by calibration against experiments on fission gas induced fuel fragmentation; see Section 3.

The fractional area coverage ϕ_2 is in our model correlated to the bubble projected radius through equations (12) and (15), which means that in our integrated model, the critical overpressure in the bubble, $P_{ex}^{cr} = P_g^{cr} - P_h - P_s$, is in fact a function of K_{Ic} and r_b only. Figure 4 shows P_{ex}^{cr} versus the bubble projected radius. It has been normalized, such that $P_{ex}^{cr} = 1$ for $r_b = r_b^o = 30\,\text{nm}$, i.e. for newly nucleated grain face bubbles. As before, $n_b^o = 3.0 \times 10^{13}\ \text{m}^{-2}$ is used in equation (12). It is clear from the figure that P_{ex}^{cr} drops by a factor of four as the bubbles grow from their assumed initial radius (30 nm) to their assumed maximum radius (325 nm). At the same time, the capillary pressure P_s drops by more than an order of magnitude. These two effects in combination make the grain boundaries more susceptible to gas induced rupture as the grain face bubbles grow, since a lower gas pressure is needed in the bubbles for the rupture to take place. From Table 3, it is clear that grain boundary rupture is assumed to cause immediate release of gas from the grain face bubbles ($\tau_2 = 0$), such that the gas pressure in the broken bubbles momentarily equals the gas pressure in the pellet-cladding gap, P_g^{gap}. Healing of the ruptured grain boundaries is not considered in the model.

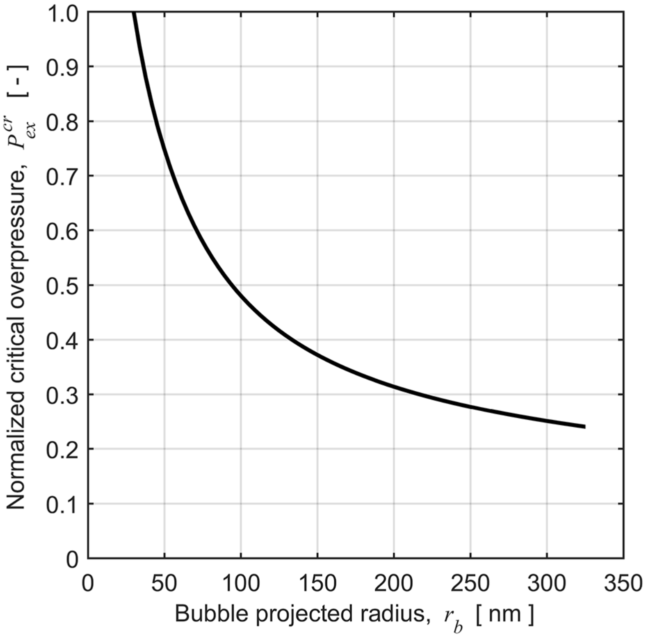

Fig. 4. Normalized critical overpressure for grain boundary rupture versus projected radius of grain face bubbles. The plot is generated by combining equations (12), (15) and (18).

(3) Grain boundary microcracking

The third mode of fission gas release considered in the model is related to formation of microcracks in the grain boundaries, through which part of the intergranular gas inventory may seep out. This release mode is assumed to be time dependent and activated when the gas pressure in grain face bubbles reaches a fraction υ of the critical pressure for complete grain boundary rupture; see Table 3. Only part of the intergranular gas inventory is vented through the tortuous network formed by the microcracks: the steady-state post-release pressure in the grain face bubbles is assumed to be υP_g^{cr}. Since P_g^{cr} decreases significantly with the fractional area coverage of grain face bubbles, the amount of gas released through the microcracks will increase with increasing ϕ_2.

The microcracking is assumed to affect only part of a grain face, and consequently, it is assumed not to cause fine fragmentation of the fuel material. Moreover, the microcracks are assumed to heal by in-reactor sintering, if the bubble gas pressure drops below υP_g^{cr}.

2.3 Evolution of pores in the high burnup structure (HBS)

The accumulation of radiation damage induces a restructuring of UO_2 and $(U,Pu)O_2$ nuclear fuel at high burnup. The restructuring is characterized by grain subdivision (polygonization) into sub-micron grains that are free of extended defects, increase in porosity and depletion of intragranular fission gas [84–86]. The high burnup microstructure is often referred to as the “rim zone structure”, since it occurs first and foremost at the pellet rim: high local burnup and fission rate in combination with low temperature promotes accumulation of radiation damage in the material at the pellet rim.

For UO_2 fuel, there is ample experimental evidence that the HBS starts to form at a local burnup of 60–70 MWd(kgU)^{-1} by subdivision of grains at the pellet outer surface and at pores and bubbles close to the surface. These numbers are approximate. A distinct burnup threshold is difficult to define, since the fuel restructuring is a gradual process, where restructured grains are reported to co-exist with original, untransformed grains up to a local burnup of 120 MWd(kgU)^{-1} [87]. The burnup threshold for restructuring is also influenced by the original grain size of the material: large-grain UO_2 materials have markedly higher resistance to restructuring than small-grain materials [88–91].

At conditions typical of LWR fuel, the pellet radial average burnup is about 45 MWd(kgU)^{-1} when the restructuring starts at the pellet rim. The fully restructured material has a typical grain size of 100–300 nm, which is much smaller than that of the original material (≈10 μm). The restructured grains are free of defects and depleted of fission gas, with the fuel matrix containing only about 10–25 % of the fission gas present within the large original grains before restructuring. More precisely, measurements by electron probe microanalysis (EPMA) have shown that the restructured grains contain 0.10–0.25 wt % (≈80–200 molm^{-3}) Xe [87,92,93]. EPMA is a local technique, by which the amount of Xe, atomistically dissolved in the fuel matrix and comprised in sub-nanometre sized intragranular bubbles, is measured within very small volumes of the material. With X-ray fluorescence (XRF) and secondary ion mass spectrometry (SIMS) techniques, it is possible to measure the average gas content in larger volumes, which comprise gas also on grain boundaries and in pores. By combining EPMA with XRF or SIMS, it has been shown that only a minor part of the fission gas that is depleted from the grain matrix is released to the rod free volume during the restructuring [92,94,95]. The major part is trapped in newly formed, micron-sized closed pores [96] that make the rim zone microstructure appear as cauliflower in micrographs [85]. Porosities in the range of 20–30 vol. % have been observed in fully restructured UO_2 with extremely high burnup [97,98], but the porosity is considerably lower for fuel with designs and burnup levels typical for commercial LWR fuel. Mechanical restraint from PCMI is known to suppress the porosity, and rim zone porosities above 15 vol % are rarely observed in commercial UO_2 fuel [93,99,100].

2.3.1 Formation of the HBS (restructuring)

The fundamental mechanisms responsible for formation and subsequent evolution of the HBS are not fully understood, and conflicting interpretations of experimental data exist in the literature, not least with regard to theoretical and empirical models [85]. Many of the models presented to date have aimed to provide a criterion for onset of HBS formation in terms of a threshold for the local fuel burnup, E. Depending on the hypotheses made for the restructuring mechanisms, the models yield different results for the burnup threshold and its dependence on key parameters, such as the fuel local temperature and fission rate [101].

Here, we apply a burnup threshold for initiation of HBS formation that combines a theoretical model by Rest [102] with an empirical relation for the influence of fuel grain size, based on the work of Une et al. [99]. The HBS formation is assumed to initiate when the local burnup E satisfies

$$E \geq E_{th} = \frac{2.94 \times 10^4}{\varphi^{2/15}} \left(\frac{S_o}{10^{-5}} \right)^{1/10}, \qquad (19)$$

where E_{th} is the local burnup threshold for initiation of HBS formation in MWd(kgU)$^{-1}$, φ is the local fission rate in fissions(m^{3}s)$^{-1}$, and S_o is the local grain size (m) of the fuel before restructuring. The reader is referred to [102] for a description of the theory behind the model, and to [101] for comparisons of the model with experimental data. It should be remarked that equation (19) is applicable to UO$_2$ fuel with an enrichment of ^{235}U less than 5 %, typical for commercial LWR fuel. The burnup threshold for restructuring is known to be significantly lower for highly enriched UO$_2$ fuel [100,103].

The burnup threshold in equation (19) is independent of fuel temperature, implying that it is applicable only to sufficiently low temperatures that thermal annealing of UO$_2$ lattice defects is insignificant [102]. Hence, for completeness, the burnup threshold must be complemented with a threshold temperature, above which annealing of defects is assumed to make fuel restructuring impossible. Kinoshita and co-workers [104] found experimentally that this threshold temperature is $1100 \pm 100\,°$C. Based on their results, we assume in our model that fuel restructuring initiates at a local fuel burnup of E_{th}, if the local fuel temperature is below 1400 K. Otherwise, the restructuring will not start until the temperature drops below this value. Modelling approaches that combine the burnup and temperature thresholds for restructuring in more elaborate ways have been proposed [103,105], but these concepts are not used here.

When the fuel restructuring is calculated to initiate at an integration point, the fission gas modelling described in Sections 2.1 and 2.2 is replaced by HBS-specific models that calculate the evolution of pore average size, number density and fission gas content. The models are empirical and based on investigations of HBS characteristics reported in open literature. More precisely, a population of equal-size spherical pores is modelled, and a large part of the fission gas content accumulated in the material is gradually transferred to these pores. The fully restructured material is assumed to approach an intragranular (matrix) gas concentration of $C_g^\infty = 150$ molm^{-3} (≈0.18 wt %). Immediately upon initiation of the restructuring, all intergranular gas and 10 % of the excess intragranular gas $(C_g - C_g^\infty)$ is assumed to escape to the newly formed pores, which are assumed to have an initial radius, r_p, of 0.5 μm. The gas pressure in the pores at time of formation is assumed to be $P_g = P_{eq} + \Delta P_o = P_h + 2\gamma_{fs}/r_p + \Delta P_o$, where ΔP_o is a constant model parameter that defines the pore overpressure at formation. It is determined such that the calculated pore gas pressure agrees with estimates from experimental studies [93,98,106,107] and also that the calculated volume fraction of porosity, $\phi_3 = n_p V_p = n_p 4\pi r_p^3/3$, in the newly formed HBS agrees with observations [93,97,100,108]. Here, the number density, n_p, of the newly formed pores is calculated from the aforementioned assumptions regarding the pore initial size, gas pressure and gas content, in combination with the local temperature at time of pore formation. Based on results from ceramographic studies of the HBS [97,98,109], the pore number density is then assumed to increase linearly with burnup, until it saturates at 10^{17} pores/m^3 at a local fuel burnup of 100 MWd(kgU)$^{-1}$. At even higher burnup, experimental data [97] show that the pore number density starts to decrease, a phenomenon attributed to Ostwald ripening [110]. This coarsening is not considered in our model.

The gradual transfer of matrix gas to the HBS pores is treated by an empirical model, similar to the one proposed for matrix Xe depletion by Lassmann and co-workers [111]. Assuming that the intragranular gas concentration is C_g^o just after HBS formation at a local burnup E_o, the concentration beyond that burnup is postulated to follow

$$C_g(E) = C_g^\infty + \left(C_g^o - C_g^\infty\right) \exp\left(-\frac{C_g^o}{C_g^\infty}\left(\frac{E}{E_o} - 1\right)\right). \qquad (20)$$

Equation (20) is compared with EPMA data for the HBS matrix Xe concentration in Figure 5. The data originate from measurements on UO$_2$ fuel pellets with average burnups from 37 to 83 MWd(kgU)$^{-1}$ [87,93,112]. The lines are calculated results from our model, which has been implemented in the FRAPCON-4.0P1 program [40]. In this example, it is applied to LWR fuel rods with various designs that have been irradiated under steady-state operating conditions to pellet average burnups up to 70 MWd(kgU)$^{-1}$; see Section 3.2.1. The calculated trajectories differ because of differences in design between the considered fuel rods, but also because the lines pertain to different axial and radial positions with different local histories of burnup, fission rate and temperature. In the calculations, it is assumed that Xe makes up 90 % of the fission gas inventory; the rest is assumed to be Kr. It is clear from Figure 5 that our model fits the upper range of the EPMA data, which exhibit a significant scatter. We consider the empirical gas depletion model in equation (20) sufficient for our purposes, but alternative approaches are available [105,113,114].

It has been established that almost all the gas that is depleted from the grains during fuel restructuring is captured in the newly formed pores, and that only a negligible fraction escapes to the rod free volume [86]. This conclusion is based on ceramographic examinations of the HBS, which generally show that the porosity is closed and not connected to the fuel free surface [96,97], and it is also corroborated by SIMS measurements on restructured fuel samples [95,106]. These measurements typically show that most of the gas produced in the fuel pellet rim region is retained in the HBS. On the other hand, there are measurements indicating that athermal fission gas release

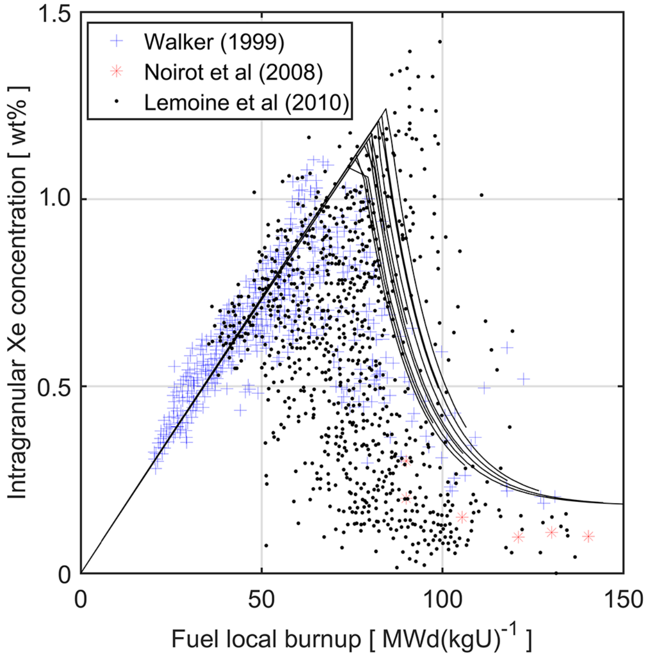

Fig. 5. Concentration of Xe in the HBS fuel matrix. EPMA data from Walker [87], Noirot et al. [93] and Lemoine et al. [112] in comparison with model results (lines) for typical LWR UO_2 fuel; see equation (20).

becomes more prominent as the fuel restructuring starts [48,94,115–117]. In our model, we assume that 80 % of the intragranular gas that is depleted during restructuring is transferred to the pores in the HBS, while the remaining 20 % is released to the rod free volume. This partitioning of gas makes the model reproduce fission gas release data from fuel rods with moderately high burnup that have been irradiated in commercial power reactors, but it does not reproduce the results of separate effect tests that have been carried out on fuel samples with non-prototypical design, which have undergone irradiation to very high burnup under non-prototypical conditions [95,104]. The fission gas release measured in this kind of tests is usually low.

2.3.2 HBS pore growth

Most of the intragranular gas that is depleted from the fuel matrix during restructuring is transferred to the HBS pores, which results in a gradually increasing pore gas pressure. Estimates of the average gas pressure in the HBS pores, based on measured porosity volume fractions and estimates of the amount of gas retained in the pores at certain local burnups, have been reported. These estimates suggest that the pore gas pressure, under normal steady-state operating conditions and at temperatures typical for the fuel pellet rim in LWRs at these conditions, is in the range from about 50 to 150 MPa [93,98,106,107,118]. This pressure span is quite large, since the estimates are based on different assumptions and input data regarding the HBS porosity, temperature and partitioning of gas between the pores and the surrounding matrix. However, it is clear that the pores are generally overpressurized also under normal operating conditions for the fuel, which leads to pore growth with increasing burnup. At the same time, the pore number density changes, which results in a complex evolution for the porosity in the HBS.

A fairly large number of experimental studies on pore growth and porosity evolution in the HBS are available in the open literature [93,97,98,100,108,109], but the phenomena are not yet fully understood. The experimental data are difficult to interpret, since characteristic properties of the HBS, such as porosity, pore size or pore number density, are presented as trends observed either with respect to local burnup or radial position in the fuel pellet. In the first case, the presented data usually pertain to different radial positions in the same pellet sample, which means that the material corresponding to the low burnup range of the data will inevitably have been exposed to higher temperature than the high burnup data, which originate from material sampled closer to the cold pellet surface. Hence, the observed trends may be a result not only of burnup, but also of temperature. On the other hand, if the data from a specific sample are presented with respect to radial position, the true burnup dependence must be established by comparing fuel pellets with different burnups. However, the results of these comparisons may be obscured by the fact that the sampled pellets differ not only with regard to burnup, but also with regard to operating history, extent of mechanical constraint by PCMI, etc.

Existing computational models for the porosity evolution in the HBS can be divided into two categories, depending on the mechanism assumed responsible for pore growth. In the first category, the HBS pores are assumed to grow by stress-directed diffusion of vacancies and interstitials to/from the pores [105,119–121]. The diffusion is caused by the gradient in hydrostatic stress that arises in the fuel material surrounding an overpressurized pore. The models are able to reproduce observed pore growth in the HBS, provided that the diffusivities applied for the point defects are increased significantly from values measured in non-restructured UO_2. For example, Blair [120] found that the athermal part of the vacancy diffusion coefficient reported for non-restructured UO_2 had to be scaled by 10^3 in order for his model to yield reasonable results. He argued that this scaling was necessary, since the diffusion of vacancies in the HBS is considerably enhanced by the high density of grain boundaries in the restructured material [120]. In the model by Khvostov and co-workers [105], similar arguments are used for increasing the point defect diffusivities of the HBS material in proportion to its degree of restructuring. The diffusion based models for HBS pore growth also require submodels for calculating the densities of irradiation induced vacancies and interstitials in the restructured material. These models are fairly complex and contain the poorly known point defect diffusivities as parameters [105,120,121].

In the second category of models [34,107,122], pore growth is attributed to generation of dislocation loops at the pore surface and subsequent movement of these loops through the fuel material, a mechanism for plastic deformation known as dislocation punching [123]. The hypothesis is experimentally supported by the very high density of dislocations observed at the pore surface by transmission electron microscopy (TEM) in the HBS [124]. Assuming that the pore grows and relaxes its overpressure by dislocation punching, a theoretical limit for the pore overpressure, P_{ex}, would be bG/r_p, where b is the Burgers vector and G is the shear modulus of the material surrounding the pore [123]. For UO_2 at 800 K, $b = 0.39$ nm and $G \approx 70$ GPa, which means that the overpressure in a pore with radius $r_p = 0.5$ μm would not exceed about 55 MPa. The aforementioned estimates of the HBS pore pressure suggest that the overpressure is about twice as high as given by this simple theoretical limit [93,98,106,107,118], but the inverse relationship with respect to pore radius seems to hold [107,118]. The pressure estimates are based on data obtained from high burnup fuel that has been irradiated under normal, steady-state operating conditions, and the data provide no information on possible kinetic effects in the presumed dislocation punching mechanism. In particular, it is unclear to what extent the pore overpressure momentarily may reach higher values under transients, as a result of time dependence in the dislocation movements.

In our model, we assume that the HBS pores grow by dislocation punching, such that the pore overpressure under steady-state operating conditions never exceeds $\Delta P_{ss} = c_{dp}/r_p$, where $c_{dp} = 55$ Nm^{-1} is the best-estimate value obtained from analysis of HBS porosity data by Gao and co-workers [107]. Under transient conditions, however, the overpressure may exceed ΔP_{ss}. Pending data on the HBS pore growth kinetics under transient conditions, we make the following simple ansatz for the pore growth rate

$$\frac{\partial r_p}{\partial t} = k_{dp} \left\langle P_{ex}(r_p) - \Delta P_{ss}(r_p) \right\rangle . \qquad (21)$$

Here, P_{ex} is the current overpressure, as defined by equation (1), $\Delta P_{ss} = c_{dp}/r_p$ is the aforementioned limit for steady-state conditions, k_{dp} is an empirical rate constant, and $<>$ denotes the Macaulay brackets. The latter ensure that $\partial r_p/\partial t \geq 0$, which means that HBS pore shrinkage is excluded in our model. Equation (21) is non-linear with regard to the pore average radius r_p. It is solved by a method, similar to that described in Appendix A for the grain face bubble volume. It contains two empirical constants, k_{dp} and c_{dp}, where the latter is fairly well determined from data on HBS characteristics in LWR fuel that has been irradiated under normal steady-state conditions [107]. Hence, the model contains far less uncertain parameters than models in which point defect diffusion is assumed to be the underlying mechanism for pore growth.

2.3.3 HBS pore venting

Two mechanisms for venting and release of the gas in HBS pores are considered in our model: (1) venting by formation of a continuous network of growing pores; (2) venting by rupture of the HBS material as a result of rapid pore overpressurization. Hence, the considered release mechanisms are similar to those discussed in Section 2.2.2 for grain boundary bubbles, but here, we do not consider gas release through a network of microcracks. The reason is that there are no obvious weak planes, similar to grain faces, that connect the HBS pores and that could serve as nucleation sites for microcracks in the restructured material. The modelling of the two release mechanisms considered for the HBS pores is presented below.

(1) Pore interconnection

If pore growth makes the porosity volume fraction increase to such an extent that an interconnected network of pores forms in the HBS, part of the pore fission gas content will be vented to the rod free volume. Analyses with percolation models of the porous material suggest that an interconnected network that allows significant gas release would form at a porosity volume fraction around 0.25–0.30 [96,125]. These theoretical thresholds agree with the highest porosity volume fractions reported from experimental investigations of the HBS in LWR UO_2 fuel with very high burnup. For example, Spino et al. [97] reported that the local porosity volume fraction was below 0.24 in all their investigated samples, which had reached local burnups as high as 240 MWd(kgU)$^{-1}$. Similarly, Restani and co-workers [98] reported peak porosity fractions of 0.24 and 0.30, observed in two different UO_2 fuel pellets with peak local burnups estimated to 240–260 MWd(kgU)$^{-1}$.

Since models and data suggest that the local porosity saturates around these values, we assume in our model that HBS pore growth ceases when the calculated porosity volume fraction reaches 0.29. Beyond this threshold, gas release by pore venting through an interconnected network is modelled by enforcing $\partial r_p/\partial t = 0$ in equation (21), leading to the condition $P_{ex} \leq \Delta P_{ss}$. Hence, below the assumed percolation threshold ($\phi_3 = 0.29$), equation (21) is used for calculating pore growth and porosity increase. When the threshold is reached, pore growth is assumed to cease and the same equation provides an upper limit for the pore overpressure, through which local fission gas release is calculated. However, fission gas release by HBS pore growth, interconnection and subsequent venting is highly unlikely at the burnup levels that are currently reached in commercial LWR fuel, since the local porosity remains well below the percolation threshold at these burnups. The aforementioned observations of local porosities in the range of 0.25–0.30 were done on UO_2 fuel with pellet average burnups in excess of 100 MWd(kgU)$^{-1}$.

(2) Pore rupture

In accident conditions, the restructured material in the pellet rim zone may rupture as a result of significant pore overpressurization, i.e. $P_{ex} >> \Delta P_{ss}$. We have chosen to model this phenomenon by use of a stress based rupture criterion. The criterion is originally derived for rupture of grain face bubbles [22] and used for this purpose in several computer programs for analyses of RIA [35–37], but according to an assessment of existing rupture criteria [81], it is applicable also to the HBS pores. More precisely, the critical pore gas pressure for rupture of the HBS can

Table 4. Properties assumed for HBS pores.

Property/parameter			Unit	Source
r_p^o	$=$	5.0×10^{-7}	[m]	[93,97,98]
c_{dp}	$=$	55	[Nm]	[107]
k_{dp}	$=$	1.0×10^{-17}	[m/(sPa)]	This work
ΔP_o	$=$	4.0×10^7	[Pa]	[93,98,106,107]
σ_{hbs}^{cr}	$=$	2.1×10^7	[Pa]	This work

be written [22,81]

$$P_g^{cr} = P_s + \frac{\sigma_{hbs}^{cr}(1-\phi_3) - \sigma_1}{\phi_3}, \tag{22}$$

where P_s is the pore capillary pressure, ϕ_3 is the pore volume fraction, σ_1 is the largest principal stress in the bulk of the porous HBS material and σ_{hbs}^{cr} is a material property that represents the local tensile strength of the solid material between the pores. This local material property has to be determined through inverse modelling, i.e. by calibration against experiments on fission gas induced fuel fragmentation. In our implementation of the rupture criterion in FRAPCON and FRAPTRAN, the largest principal stress σ_1 in equation (22) is replaced with $-P_h$, i.e. the calculated hydrostatic stress. The reason is that the fuel pellet stress state is not calculated by these computer programs [40,41]; see Section 3.1.3. Moreover, pore rupture is in the model assumed to cause immediate gas release, such that the gas pressure in the broken pores equals the gap gas pressure. The intragranular gas inventory is not affected: it is assumed to follow equation (20) also after pore rupture. The model parameters applied for HBS pores are summarized in Table 4.

3 Model validation against experiments

3.1 Basis for the validation

3.1.1 Applied computer programs

The models described in Section 2 have been implemented in the FRAPTRAN-1.5 and FRAPCON-4.0P1 fuel rod analysis programs [40,41] and validated against experiments. FRAPTRAN is intended specifically for analysing the fuel rod thermal-mechanical behaviour in LWR transient and accident conditions. Since the program lacks models for long-term steady-state fuel operation, it requires that burnup-dependent pre-accident fuel rod conditions are defined as input. This input is usually generated by use of FRAPCON, which is a sibling program designed for fuel rod thermal-mechanical analyses of normal, steady-state fuel operation. If the programs are used together, the burnup-dependent data needed as input by FRAPTRAN are transferred from FRAPCON via an interface.

The models presented in Section 2 were introduced in our in-house versions, named FRAPCON-QT-4.0P1 and FRAPTRAN-QT-1.5. The latter program differs substantially from the original version developed by the Pacific Northwest National Laboratory (PNNL), USA, since it has been extended with additional and alternative models in earlier projects [42]. We have also extended the interface between our versions of FRAPCON and FRAPTRAN to include all data produced by the models in Section 2 regarding fission gas distribution, grain face bubbles and HBS pores. These models are identical in our versions of FRAPCON and FRAPTRAN, to avoid problems related to the transition from modelling of steady-state operation to transients or accidents.

Most of the models presented in Section 2 have been separately calibrated and validated against experimental data before introducing them in FRAPCON-QT-4.0P1 and FRAPTRAN-QT-1.5. Here, we will therefore focus on integral validation of the models, i.e. how the models play together and how they perform together with existing models in the two programs. There are also a few material properties and model parameters that have to be determined by inverse modelling, i.e. by calibrating the models against results from separate effect tests and/or integral-type experiments. Among these properties are the local fracture energy for the grain boundaries and the local tensile strength for the restructured fuel material in the pellet rim zone; see Sections 2.2.2 and 2.3.3.

3.1.2 Assumed material properties

All calculations in this paper were performed with material properties and model parameters as defined in Tables 1–4. Thermo-elastic properties of UO_2 fuel (E_Y, ν and α_1) were calculated through correlations in the FRAPCON and FRAPTRAN programs, which make use of the MATPRO [126] material property library.

The diffusivities, both for fission gas atoms in the grain and for uranium vacancies in the grain boundaries, are important material properties in our models. Unfortunately, large differences exist between correlations presented for the fission gas atom diffusivity; see e.g. the works by Lawrence [127] and Kogai [70], who also discuss the reasons for these differences. In our model for intragranular gas diffusion, we apply a widely used correlation for the lattice diffusivity of gas atoms [49,50] in combination with a simple semi-empirical model for the attenuation of the diffusivity by gas trapping in intragranular bubbles [52]; see Section 2.1.1. The resulting effective gas atom diffusivity, D_{eff}, involves uncertainties related to both models. Uncertainties also exist for the vacancy diffusivity in UO_2 grain boundaries. Experimental data for D_{gb}^v in the temperature range 1500–2200 K have been presented by Reynolds and Burton [128] and by White [62]. The activation energies reported for D_{gb}^v in these two studies are similar, but the magnitude of D_{gb}^v differs by about two orders of magnitude [62]. To the author's knowledge, no data on D_{gb}^v are available for lower temperatures or for possible radiation enhancement effects, which may be important at low temperature. In lack of such data, we assume that the vacancy diffusivity follows about the same trends with respect to temperature and fission rate as the diffusivity of Xe and other inert fission gases in UO_2. This assumption is based on the hypothesis that Xe migration is assisted by uranium vacancies, which is well established for bulk diffusion and to some extent also for grain boundary diffusion; see e.g. [129,130] and references therein. The connection between diffusion of Xe atoms and uranium vacancies in UO_2 was used by Kogai [70], who assumed that they had the same grain boundary diffusivity that could be calculated through $D_{gb}^{v} = D_{gb}^{Xe} = 6.9 \times 10^{-4} \exp(-38770/T)$. This correlation is an improved fit to the data by Reynolds and Burton [128]. In our application of the Speight-Beeré model, we use this expression for the grain boundary vacancy diffusivity, complemented with low-temperature terms taken from the applied correlation for fission gas atom lattice diffusivity; confer D_l and D_{gb}^{v} in Tables 1 and 2. The applied correlation constitutes a rough estimate for D_{gb}^{v} in the low temperature (<1500 K) regime, justified only by the observed similarity in diffusivity between fission gas atoms and uranium vacancies in UO_2.

3.1.3 Estimated stress state

The fuel pellet stress state is needed as space-time dependent input from the host code to the models in Section 2. Since neither FRAPCON nor FRAPTRAN calculates stresses in the fuel pellet, we estimate $P_h = -\text{trace}(\boldsymbol{\sigma})/3$ from other parameters as follows: For steady-state operating conditions, it is reasonable to believe that stresses, induced by differential thermal expansion and swelling because of the radial temperature gradient in the pellet, are relaxed by creep and do not significantly affect the local stress state. Hence, in FRAPCON-QT-4.0P1, we assume that the hydrostatic pressure is uniform across the pellet radius and given by

$$P_h(t,z) = P_g^{gap}(t) + \frac{2}{3} P_c^{gap}(t,z), \tag{23}$$

where P_g^{gap} is the gas pressure in the pellet-cladding gap and P_c^{gap} is the pellet-cladding contact pressure. These pressures are calculated by FRAPCON. While equation (23) is deemed a reasonable approximation for steady-state conditions, it does not apply to transient conditions where creep and viscoplasticity may not be fast enough to relax local thermal stresses in the fuel fragments. Assuming a thermo-elastic transient response by the pellet fragments [131], the magnitude of local thermal stresses will be proportional to $\alpha_1 E_Y l_r |\partial T/\partial r|$, where α_1 and E_Y are the coefficient of linear thermal expansion and Young's modulus of the fuel material and l_r is the radial extension of the considered fragment. The thermal stresses will be compressive in the hot end of the fragment and tensile in the cold end. Since the tensile part will promote growth and rupture of grain face bubbles and HBS pores, we estimate the local hydrostatic pressure in the fuel pellet under transients through

$$\begin{aligned} P_h(t,r,z) = {} & P_g^{gap}(t) + \frac{2}{3} P_c^{gap}(t,z) \\ & - c_{th}\alpha_1 E_Y \left| \frac{\partial T(t,r,z)}{\partial r} \right| . \end{aligned} \tag{24}$$

Equation (24) is used for estimating P_h in FRAPTRAN-QT-1.5. The parameter c_{th} was determined by model calibration against RIA simulation experiments, where significant radial temperature gradients arise rapidly in the fuel pellet. The value used in all calculations was $c_{th} = 2.0 \times 10^{-5}$ m.

3.2 Results

Examples where the implemented models in FRAPCON-QT-4.0P1 and FRAPTRAN-QT-1.5 are validated against open literature experimental data are presented below. The selected examples comprise experiments on steady-state fuel operation, loss-of-coolant accidents and reactivity initiated accidents. They are intended to illustrate the modelling approach and the performance of the models.

3.2.1 Normal steady-state conditions

Accurate modelling of the fission gas behaviour under normal steady-state conditions is a prerequisite for our integrated approach to modelling gas induced fuel fragmentation and TFGR under accident conditions. The long-term buildup of grain face bubbles and HBS pores, along with the partitioning of fission gas between the bubbles, pores and the fuel matrix, has to be modelled with sufficient fidelity and detail to provide the initial conditions for a simulated accident scenario. For this reason, we have validated the models in Section 2 by comparing calculated results from FRAPCON-QT-4.0P1 with fission gas data from post-irradiation examination (PIE) of UO_2 fuel rods that have been operated under steady-state conditions. As an example, Figure 6 shows a comparison of calculated and measured end-of-life (EOL) fission gas release fractions for 20 UO_2 fuel rods that belong to the steady-state FGR assessment database for FRAPCON-4.0 [132]. These rods represent a wide range of LWR fuel designs and operating conditions, with EOL rod average burnups from 2.6 to 70 MWd(kgU)$^{-1}$. They were operated under steady-state conditions with maximum rod average linear heat generation rates (LHGRs) between 23 and 58 kWm^{-1}, and the measured EOL fission gas release fractions range from 0.8 to 48 %. In Figure 6, calculated results are shown for our set of models from Section 2 and also for the standard (MASSIH) FGR model in FRAPCON-4.0 [40]. The L^1 norm of relative deviations between calculated and measured EOL FGR for the 20 rods shown in Figure 6 is 3.18 for the MASSIH model and 3.64 for our set of models, giving average relative deviations (absolute values) of 16 and 18 %, respectively. Hence, the MASSIH model reproduces the considered data with slightly higher fidelity than our set of models. This is not surprising, since key parameters in the MASSIH model, such as fission gas diffusivity, are calibrated against the FGR experiments shown in Figure 6. On the other hand, the only model parameter with relevance to steady-state fission gas release that has been calibrated in our set of models is a single scalar coefficient for the grain boundary resolution rate; see B_{gb} in Table 1. The resolution rate controls the partitioning of fission gas between the grain

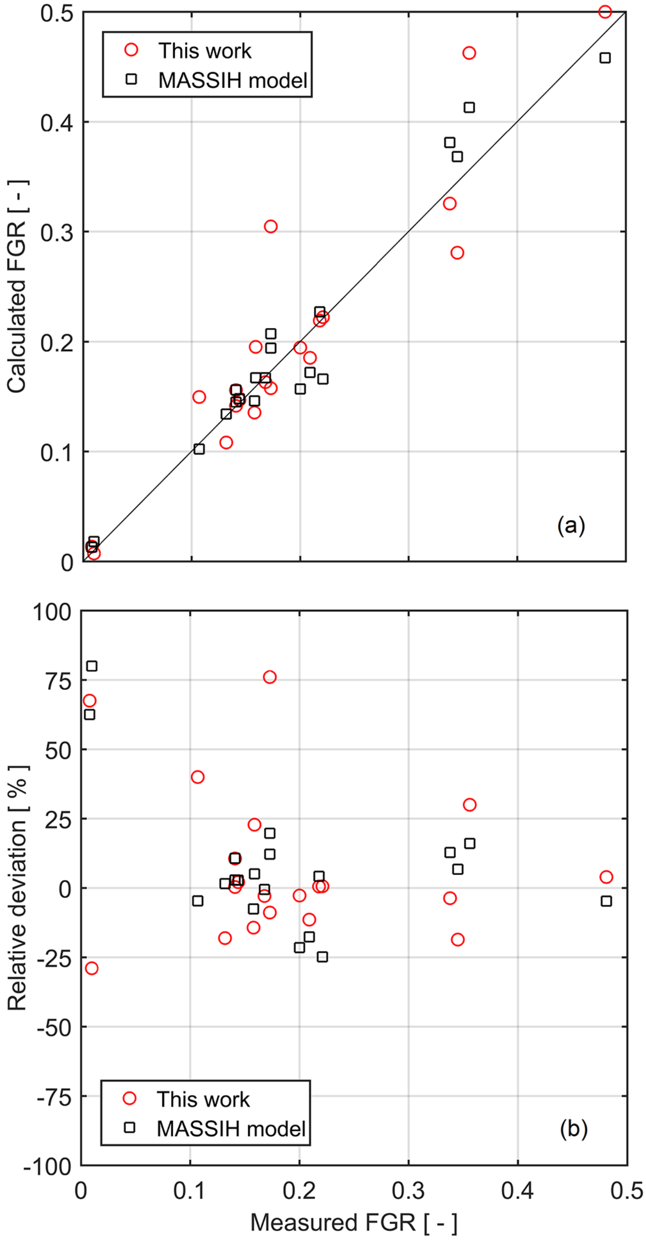

Fig. 6. Comparison of calculated and measured EOL FGR fractions for UO_2 fuel rods in the FRAPCON-4.0 steady-state FGR assessment database [132].

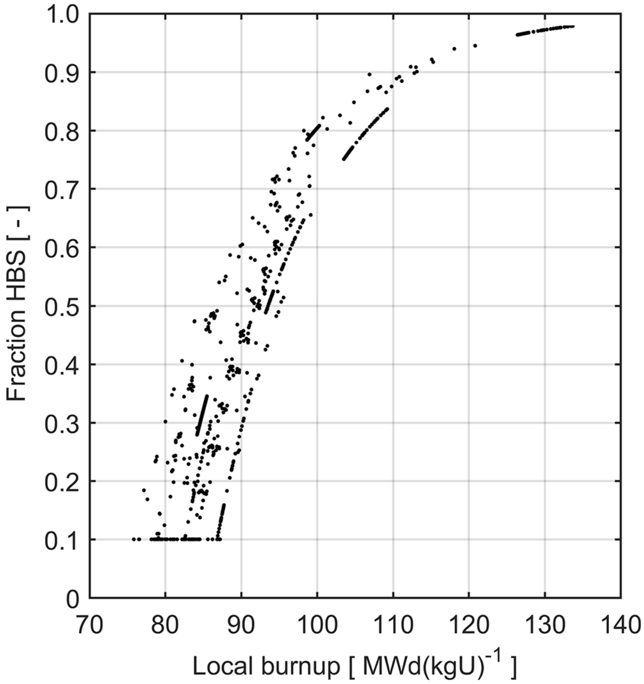

Fig. 7. Calculated fraction of restructured material in the fuel pellet rim zone versus local burnup. The model in Section 2.3 is applied to UO_2 fuel rods in the FRAPCON-4.0 steady-state FGR assessment database [132].

and the grain boundary; see equation (9). It is obvious from Figure 6b that the relative deviations for both models are within ±25 % for most of the cases, but outliers exist.

Figure 7 shows the calculated fraction of high burnup restructuring versus local fuel burnup, evaluated for the same set of fuel rods as considered above. The fraction of restructured material, ψ, is calculated from $\psi = (C_g^o - C_g)/(C_g^o - C_g^\infty)$, where the intragranular gas concentrations C_g, C_g^o and C_g^∞ are defined in equation (20). Each dot in the plot represents a specific point in space and time for a specific fuel rod, and the scatter is due mainly to the differences in local temperature and fission rate, but also to differences in fuel enrichment and grain size between the rods; see Section 2.3.1. According to our model, fuel restructuring is suppressed as long as the local fuel temperature remains high (>1400 K). When the temperature eventually drops below this threshold as a result of coast-down reactor operation, restructuring will occur. Hence, it will start at a higher local burnup than what is normally the case for the colder, peripheral part of the fuel pellet. This effect is clearly seen in Figure 7.

3.2.2 Loss-of-coolant accident conditions

As an example of model validation against LOCA tests, we consider two integral tests on high burnup PWR fuel rods in the Halden reactor IFA-650 test series. This test series specifically addresses fragmentation, axial relocation and dispersal of high burnup LWR fuel in LOCA conditions [26]. Other example applications of the models in Section 2 to LOCA tests can be found elsewhere [133].

More specifically, we consider here tests 9 and 10 in the Halden IFA-650 series. These tests have recently been used as a basis for an international computer code benchmark [134,135] and detailed information on the tests will shortly be made available through the International Fuel Performance Experiments (IFPE) database [136]. Both tests were done on single fuel rodlets, sampled from full-length UO_2 fuel rods that had been irradiated to high burnup in two different commercial PWRs. The design and pre-irradiation conditions of the two test rods thus differ; the reader is referred to [135,136] for details. Figure 8 shows the irradiation histories for the 440–480 mm long

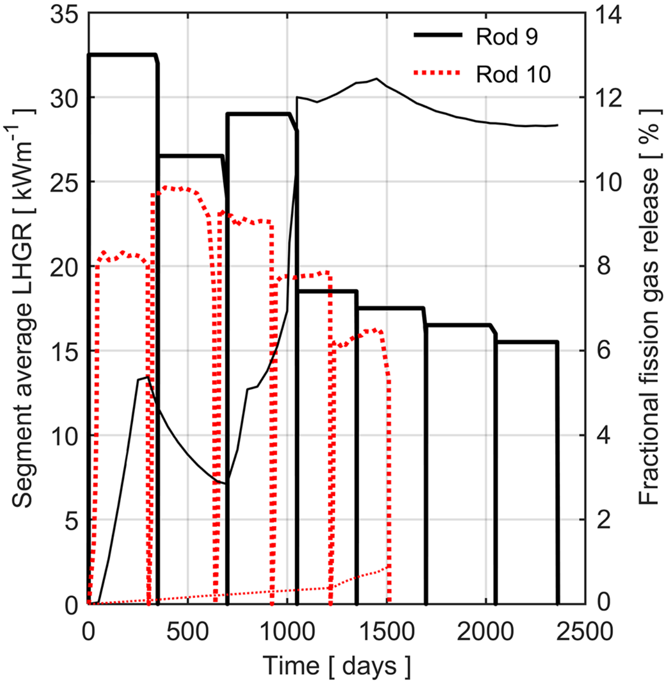

Fig. 8. Thick lines: Irradiation histories for the fuel rod axial segments that were refabricated into the Halden IFA-650.9 and IFA-650.10 test rodlets [135]. Thin lines: Calculated fission gas release from the segments.

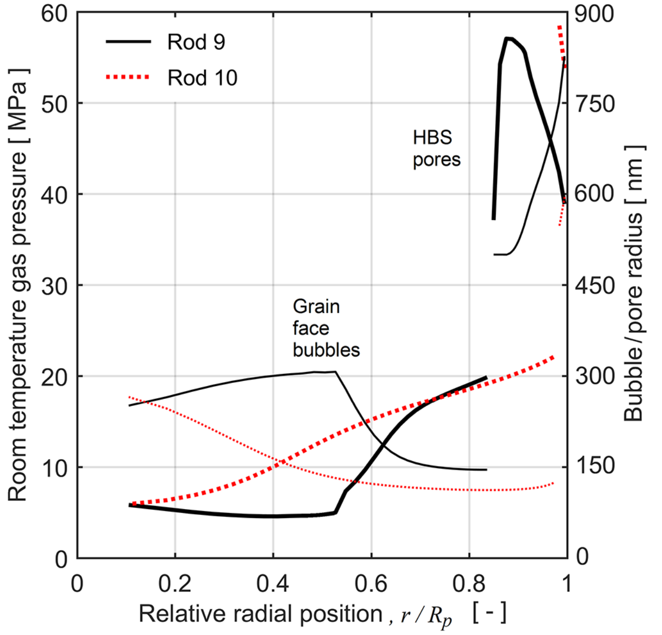

Fig. 9. Calculated pre-test conditions for the Halden IFA-650.9 and IFA-650.10 test rodlets. Thick lines: Gas pressure in grain face bubbles and HBS pores. Thin lines: Average radius of grain face bubbles and HBS pores. R_p: Fuel pellet radius.

axial segments of the mother rods that were refabricated into test rodlets. The end-of-life burnup was 89.9 and 61.0 MWd(kgU)$^{-1}$, respectively, for the two segments. Rod 9 experienced high LHGR during the first three reactor cycles, leading to thermal fission gas release. The average fractional gas release for the two segments, calculated versus time by use of FRAPCON-QT-4.0P1 with the models in Section 2, is plotted in Figure 8.

Due to the differences in pre-irradiation conditions, the two test rodlets differ with regard to pre-test distributions of fission gas, grain face bubbles and HBS pores. This is illustrated in Figure 9, which shows key pre-test conditions versus radial position in the fuel pellet, as calculated with the models in Section 2, implemented in FRAPCON-QT-4.0P1. The calculations suggest that rod 9 has a wide rim zone with large pores in its outer part. In the fuel pellet interior ($r/R_p < 0.52$), grain face bubbles have grown and formed an interconnected network, much of the grain boundary gas has been released, and the bubble gas pressure is low. However, in the late part of the irradiation history, the once-vented grain face bubbles have shrunk and re-closed. The calculated results for rod 10, on the other hand, show a narrow ($\approx$50 μm) rim zone, where the average pore radius is just below 600 nm. In the fuel pellet interior, grain face bubbles have grown to an average radius of at most 280 nm, which in our model is insufficient to form interconnected release paths for the grain boundary gas. Hence, there is no calculated thermal fission gas release for rod 10. The maximum room temperature gas pressure in the grain face bubbles is calculated just inside the restructured rim zone and amounts to about 20 MPa for both rods. Likewise, the maximum room temperature gas pressure in the HBS pores is calculated to be 60 MPa before the LOCA tests.

Each Halden IFA-650 LOCA test was conducted on a single instrumented test rodlet, which was surrounded by an electrically heated shroud and a pressure flask. The pressure flask was placed in one of the experimental channels of the Halden reactor and connected to a circulated loop with water at 7 MPa and 515 K. After preconditioning the rodlet at steady power for 7–8 hours, the LOCA test was initiated by opening valves from the test loop to a blowdown tank. Following a 30–70 s long blowdown phase, the test rodlet heated up with a rate controlled by the predetermined power levels of the rodlet and the electrically heated shroud. When the target temperature was reached, the test was terminated by switching off the electrical heater and scramming the reactor. The test rodlet was then left to cool down slowly, without quenching, in order to maintain as far as possible the conditions obtained during the high temperature phase. After the test, the rodlet was extensively investigated, in particular with regard to the cladding degradation and the fuel fragmentation and relocation behaviour [26,135].

Cladding tube rupture occurred earlier in test 9 than in test 10, because of a higher heat load and a shorter blowdown phase in the former test; key parameters for the two tests are summarized in Table 5. Significant fuel pellet fine fragmentation and axial relocation of pellet fragments were reported for test rodlet 9, whereas only limited fine fragmentation and relocation was observed for rodlet 10 [26,135]. These results are fairly well reproduced by the models presented in Section 2, which have been used in our simulations of the tests with FRAPTRAN-QT-1.5.

Table 5. Summary of Halden LOCA tests IFA-650.9 and IFA-650.10 [135]. The indicated time and axial position of cladding burst refer to start of blowdown and bottom end of the fuel pellet column.

		Rod 9	Rod 10
Test rodlet characteristics			
Cladding material		Zr-4*	Zr-4
Cladding oxide thickness	[μm]	7-8	27-30
Fill gas pressure at 295 K	[MPa]	4.0	4.0
Average fuel burnup	[MWd/(kgU)]	90	61
Testing conditions			
Rodlet LHGR	[kW/m]	2.60	1.37
Heater LHGR (initial)	[kW/m]	1.60	1.20
Blowdown duration	[s]	35	71
Peak cladding temperature	[K]	1475	1114
Cladding burst time	[s]	133	249
Cladding burst position	[mm]	80	240

* DUPLEX cladding with outer liner of Zr-2.5 wt %Nb.

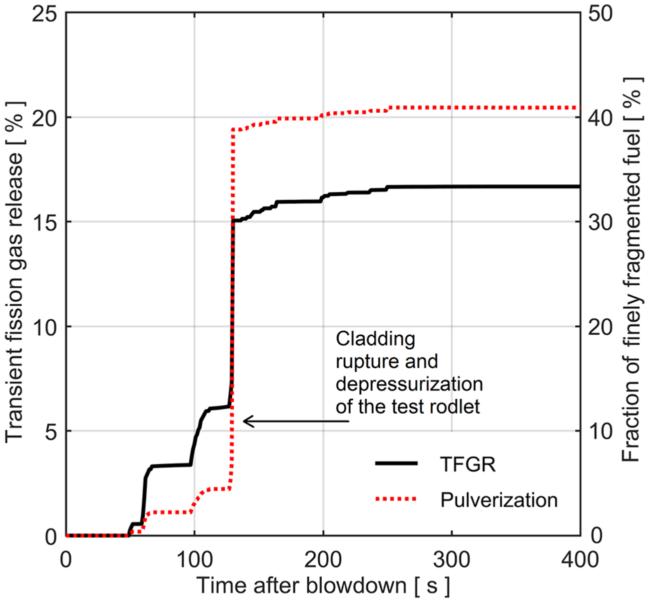

Fig. 10. Calculated evolution of rodlet average transient fission gas release and fuel pellet pulverization for test IFA-650.9.

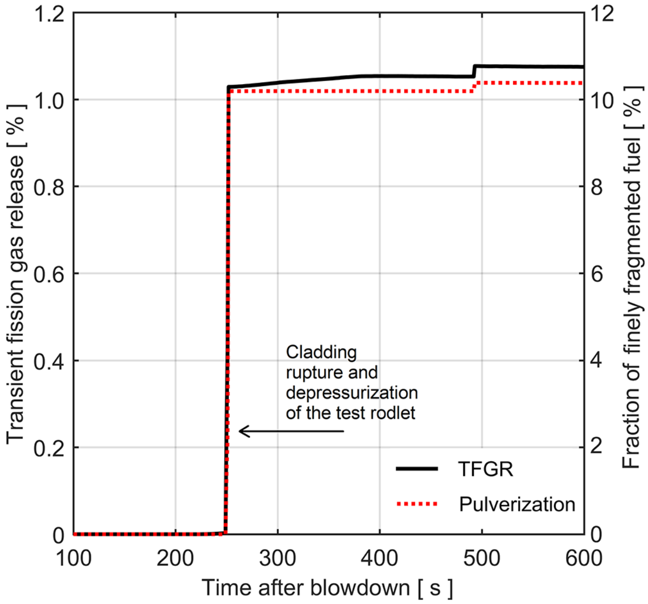

Fig. 11. Calculated evolution of rodlet average transient fission gas release and fuel pellet pulverization for test IFA-650.10.

The methodology and the general results of these simulations are described in [42]. Figures 10 and 11 show the calculated rodlet average fractions of transient fission gas release and fuel fine fragmentation (pulverization) versus time for the two tests. The calculated results can be summarized as follows: For rod 9, fuel fine fragmentation and TFGR start about 50 s after blowdown by rupture of overpressurized HBS pores at the pellet surface. The calculated pre-test porosity at the pellet surface is about 24 %. This makes the material susceptible to heating, and the local fuel temperature at first occurrence of HBS pore rupture is about 800 K.

As the heating continues, the fuel pulverization and its associated fission gas release progress both axially along the rod and radially further into the HBS. The step-like shape of the curves in Figure 10 for $50 < t < 130$ s is an artefact, caused by the spatial discretization of the restructured rim zone in our calculations. The fuel pulverization is fairly moderate until the cladding ruptures and the rod internal gas pressure drops from 5.9 to 0.3 MPa. In our calculations, this pressure drop is simplistically assumed to occur instantaneously along the entire test rodlet [42]. The sudden loss of confining hydrostatic pressure on the fuel pellets triggers significant pulverization, not only of the HBS, but also of material subjacent to the restructured pellet rim. The rodlet average fraction of pulverized fuel increases momentaneously from 5 to 39 % as the confining pressure is lost; see Figure 10. The fraction then increases gradually to about 41 % as the fuel temperature increases. This late pulverization occurs mostly by pore rupture in the partly restructured material of the pellet rim, where the porosity is moderate.

For rod 10, our calculations indicate only moderate fuel pulverization and transient fission gas release. As shown in Figure 11, the calculated pulverization and TFGR start when cladding integrity is lost and the rod internal gas pressure drops from 6.4 to 0.4 MPa. This sudden drop in hydrostatic pressure triggers pulverization of non-restructured material just inside the pellet rim zone. The pulverization occurs mainly by rupture of overpressurized grain face bubbles, and it results in a rodlet average fraction of pulverized fuel of about 10 %. The grain boundary rupture leads to a rodlet average TFGR of only 1.1 %, since the concentration of grain boundary gas in the outer part of the fuel pellet is low. Rupture of pores in the HBS would lead to much larger gas release, but according to our calculations, HBS pore rupture is very limited in rodlet 10. The reason is that the calculated HBS porosity (ϕ_3) is below 10 vol %, which implies that the critical pore gas pressure for rupture of the restructured material is fairly high; see equation (22). From Figure 11, we note a sudden jump in the calculated pulverization and TFGR at $t \approx 490$ s. This is caused by thermal gradients induced in the fuel pellet during cool-down; the test was terminated by reactor scram at $t = 417$ s [135].

In conclusion, our calculated results for the Halden IFA-650 LOCA tests 9 and 10 are in line with the reported outcome of the experiments. In particular, the observed differences between the two test rodlets with regard to fuel pulverization are captured by the models introduced in FRAPTRAN-QT-1.5. The calculated fractions of pulverized fuel differ by a factor of four, and the calculated fractions of released fission gas differ by a factor of thirty between the rodlets. This suggests that the calculated release fractions depend not only on the fractions of pulverized fuel, but also on what part of the fuel pellet is pulverized: rupture of the HBS pores leads to larger TFGR per volume pulverized fuel than grain boundary rupture in the non-restructured fuel material.

3.2.3 Reactivity initiated accident conditions

The models in Section 2 have been validated against RIA simulation tests on high burnup LWR fuel. As an example, we consider here two tests, REP-Na11 and CIP0-1, that were conducted in the CABRI facility, Cadarache, France, under very similar testing conditions. The test rodlets, however, differed with regard to their pre-test conditions, since they were sampled from two different full-length 17 × 17 design UO_2 PWR fuel rods that had been operated for five reactor cycles in two different commercial PWRs. The most important characteristics of the test rodlets are summarized in Table 6, together with the testing conditions. Further information is available in [137,138].

The pre-test conditions were calculated by simulating the irradiation histories of the mother rods with FRAPCON-QT-4.0P1. Figure 12 shows the calculated variation of average bubble/pore size and bubble/pore gas pressure across the pellet radius for the sampled segments that were re-fabricated into 540–560 mm long test rodlets. CIP0-1 was pre-irradiated with a higher heat load than REP-Na11, which explains the difference in calculated grain face bubble size between the two rodlets. According to our calculations, no thermal fission gas release occurred during pre-irradiation of the REP-Na11 rodlet, whereas CIP0-1 experienced some thermal release from the pellet centre: the calculated pre-test release fractions were 0.8 and 6 % for the two rodlets. We also note from Figure 12 that the CIP0-1 rodlet had a significantly wider rim zone than REP-Na11, due to its higher burnup.

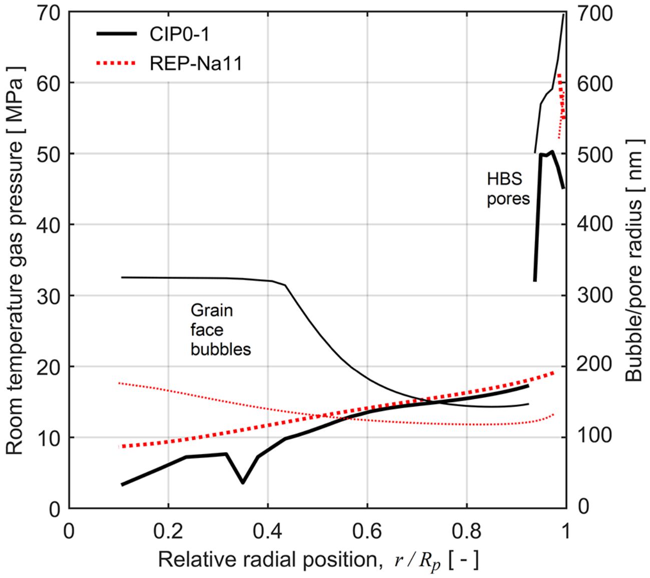

Fig. 12. Calculated pre-test conditions for the CABRI CIP0-1 and REP-Na11 test rodlets. Thick lines: Gas pressure in grain face bubbles and HBS pores. Thin lines: Average radius of grain face bubbles and HBS pores. R_p: Fuel pellet radius.

The considered RIA simulation tests were done in the former sodium loop of the CABRI reactor, which means that the test rodlets were cooled by flowing sodium with an initial temperature and pressure of 553 K and 0.3 MPa. The rodlets were pulse-irradiated with very similar power pulses, which reached their peak values about 0.44 s after test initiation. The rodlets survived the tests without cladding failure, and post-test investigations revealed that the cladding peak hoop plastic strain resulting from the test was 0.4–0.5 % for both rodlets [137,138]. The TFGR resulting from the test, measured by rod puncturing, was 15 % for CIP0-1 and 6.8 % for REP-Na11 [137,138]

These reported values for transient fission gas release should be compared with calculated results from our simulations of the tests with FRAPTRAN-QT-1.5, which are 9.3 and 3.2 %, respectively. Hence, the calculated release fractions are about half of those measured, but the large difference between the two tests is captured by the model. Figures 13 and 14 show the calculated rodlet average fractions of TFGR and fuel fine fragmentation versus time for the two tests. The calculated results for the two rodlets are similar in that nearly all fine fuel fragmentation and fission gas release occur within 0.3 s after the power pulse at $t = 0.44$ s. For both rodlets, the pulverization starts at the pellet surface in the peak power axial position and then progresses both axially and radially. For CIP0-1, further fragmentation and TFGR are calculated over the time span from 3.3 to 5.8 s. This is caused by a significant

Table 6. Summary of CABRI RIA tests REP-Na11 and CIP0-1 [137,138].

		REP-Na11	CIP0-1
Test rodlet characteristics			
Cladding material		M5	ZIRLO
Cladding oxide thickness	[μm]	15-25	50-100
Fill gas pressure at 295 K	[MPa]	0.3	0.3
Average fuel burnup	[MWd/(kgU)]	60	75
Testing conditions			
Power pulse width (FWHM)	[ms]	31	32
Timing of peak power	[s]	0.446	0.437
Peak fuel pellet enthalpy	[J/(gUO$_2$)]	385	389

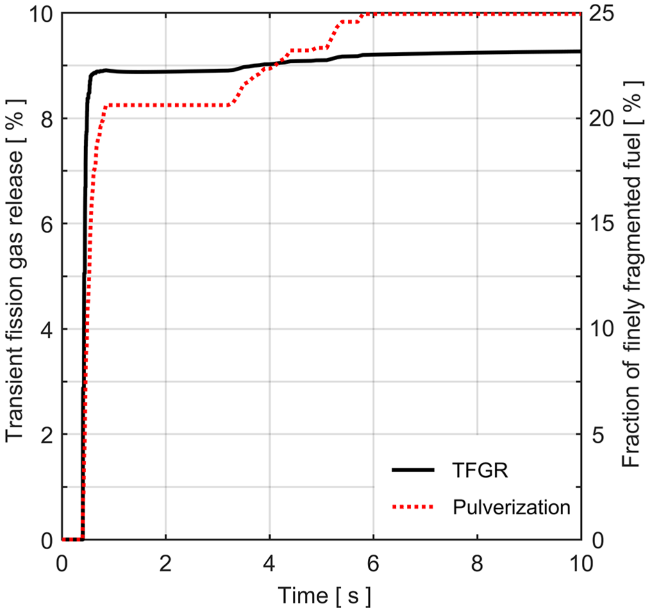

Fig. 13. Calculated evolution of rodlet average transient fission gas release and fuel pellet pulverization for test CIP0-1.

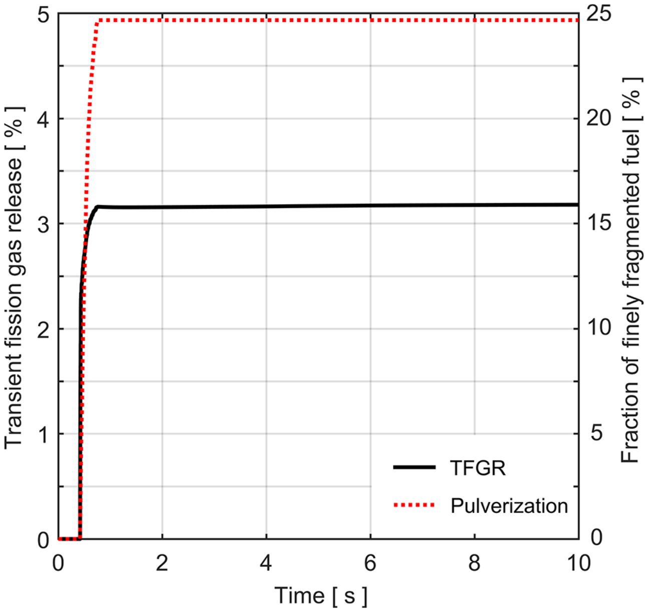

Fig. 14. Calculated evolution of rodlet average transient fission gas release and fuel pellet pulverization for test REP-Na11.

relaxation of the pellet-cladding contact pressure in this time interval, followed by opening of the pellet-cladding gap when the rodlet temperature returns to 553 K after the power pulse. The late fragmentation is concentrated to the central third of the CIP0-1 rodlet; see Figure 15.

The calculated post-test fractions of pulverized fuel (rodlet averages) are about 25 % for both CIP0-1 and REP-Na11. This means that, on average, the calculated zone with finely fragmented fuel material extends to a depth of approximately 0.5 mm from the pellet surface. However, the extent of fuel fine fragmentation varies significantly along the test rodlets, which is shown in Figure 15. In the figure, the calculated axial variation of fine fuel fragmentation is compared with the axial power profile for each test. CIP0-1, but not REP-Na11, has a distinct peak in the calculated fraction of finely fragmented fuel at the peak power axial position. This peak develops late in the test, more specifically in the time span from 3.3 to 5.8 s. It is related to the aforementioned relaxation of the pellet-cladding contact pressure, which triggers pulverization of non-restructured material beneath the pellet rim zone. The peak results from a combination of high fuel temperature, causing a high gas pressure in grain face bubbles, and a rapid relaxation of the pellet-cladding contact pressure at the peak power axial position of the rodlet.

Considering the difference in burnup between the rodlets, it may seem somewhat surprising that the calculated average fractions of finely fragmented fuel are comparable for REP-Na11 and CIP0-1. However, REP-Na11 experiences milder PCMI during the test than CIP0-1, due to the lower burnup and a cladding material with lower yield strength. REP-Na11 also has a much thinner cladding oxide layer than CIP0-1, which leads to a steeper fuel radial temperature gradient that in our model affects the local stress state; see equation (24). In combination, the milder PCMI and the steeper temperature gradient reduces the local hydrostatic pressure in the fuel, which in our model favours fuel fine fragmentation for REP-Na11.

Since rupture of porous fuel material in the HBS releases more fission gas than rupture of an equivalent

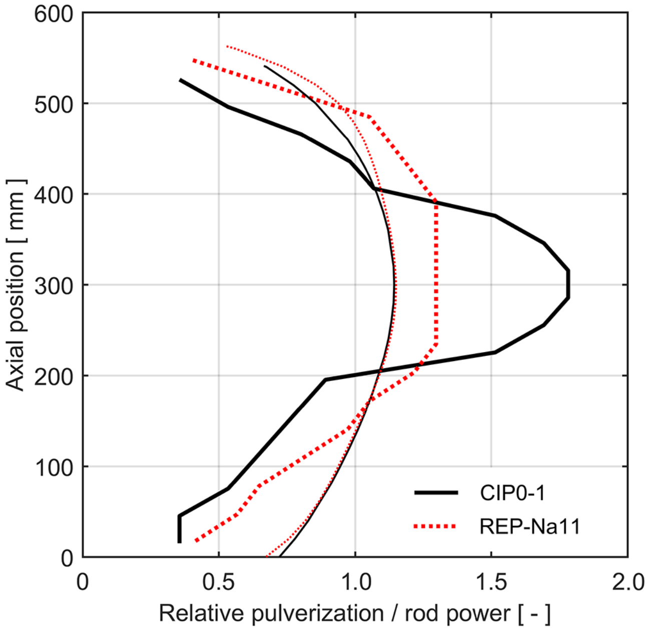

Fig. 15. Thick lines: Calculated fraction of finely fragmented fuel, normalized with the rodlet average value. Thin lines: Axial power profile used in the test.

volume of non-restructured material, the transient fission gas release is most pronounced when the pellet rim zone ruptures. As the pulverization progresses into the subjacent non-restructured material, the associated fission gas release is more moderate. This calculated behaviour is particularly clear for the REP-Na11 test rodlet, which had a narrow rim zone. Accordingly, the calculated TFGR for REP-Na11 is just one third of that for CIP0-1, notwithstanding similar calculated fractions of finely fragmented fuel. Hence, as in Section 3.2.2, we conclude that the extent of fuel restructuring has a strong impact on the transient fission gas release.

4 Conclusions and outlook

The purpose of the presented work was to integrate rupture criteria for two kinds of gas filled cavities in UO_2 fuel, viz. intergranular bubbles and HBS pores, with computational models that provide the necessary input to these criteria. More precisely, the models are used for calculating the distribution of gaseous fission products and the evolution of microstructure in UO_2 fuel with regard to intergranular bubbles and HBS pores under long-term steady-state reactor operation and transients. The proposed models are intended for implementation in engineering type computer programs for thermal-mechanical analyses of LWR fuel rods, and their level of detail is adapted to other models typically found in such programs. In particular, the proposed models depend on the host code for generating necessary boundary conditions in terms of the space-time variation of fuel temperature, mechanical stress state and fission gas production.

4.1 Summary of main findings

The presented models have been implemented in our in-house versions of the FRAPCON-4.0P1 and FRAPTRAN-1.5 fuel rod analysis programs and validated against LOCA and RIA integral tests on high burnup LWR fuel rods. The purpose of the validation was partly to determine the local fracture properties and other key model parameters by calibration against experimental data on fuel fine fragmentation and transient fission gas release. As illustrated by the selected validation cases in Section 3.2, the models give plausible results for fuel fine fragmentation and TFGR for both LOCA and RIA conditions. The fragmentation with its associated gas release may occur both in the restructured rim zone and in the non-restructured material subjacent to this zone. Local properties of the material, such as size, number density and fission gas content of grain face bubbles and HBS pores, together with the thermal-mechanical loading of the fuel during the accident, determine where and when the fragmentation occurs. The aforementioned local properties of the material evolve by complex processes during the entire lifetime of the fuel, and the computational models in Section 2 provide reasonable estimates for the evolution of fuel microstructure and fission gas distribution for a given operating history. The computational load entailed by the models is dominated by the solution of the stiff differential equations for bubble and pore growth; see Appendix A. The computational load depends strongly on the case analysed, but on average, the models increase the execution times of the FRAPCON and FRAPTRAN programmes by about 50 %.

The calculated results suggest that the extent of fuel fine fragmentation and TFGR depends strongly on the pre-accident state of the fuel, and in particular, we find that transient fission gas release is enhanced when the pellet average burnup exceeds about 60 MWd$(kgU)^{-1}$. From Sections 3.2.2 and 3.2.3, it is clear that the calculated TFGR is moderate for the test rods with fuel burnup around 60 MWd$(kgU)^{-1}$, but significant for the rods with extreme burnup, i.e. $\geq$ 75 MWd$(kgU)^{-1}$. According to our model, this is mainly because of the much wider rim zone with porous high burnup structure. Fission gas release caused by fine fragmentation of the material is calculated to occur both in the restructured material at the pellet rim and in the original material subjacent to the rim, but rupture of the porous rim material releases significantly more fission gas than rupture of an equivalent volume of non-restructured material.

The marked increase in calculated TFGR for fuel burnups in excess of about 60 MWd$(kgU)^{-1}$ is supported by experimental data from RIA simulation tests, carried out on pre-irradiated UO_2 LWR fuel. These data are shown in Figure 16, from which it is clear that test rods with a burnup in excess of 60 MWd$(kgU)^{-1}$ generally have higher release fractions than those with lower burnup. This threshold-type burnup dependence is considered in recently proposed regulatory guides for radiological analyses of RIAs [139]. For rods with burnup less than 60 MWd$(kgU)^{-1}$, the correlation between TFGR and fuel burnup is weak; see Figure 16. This is consistent with

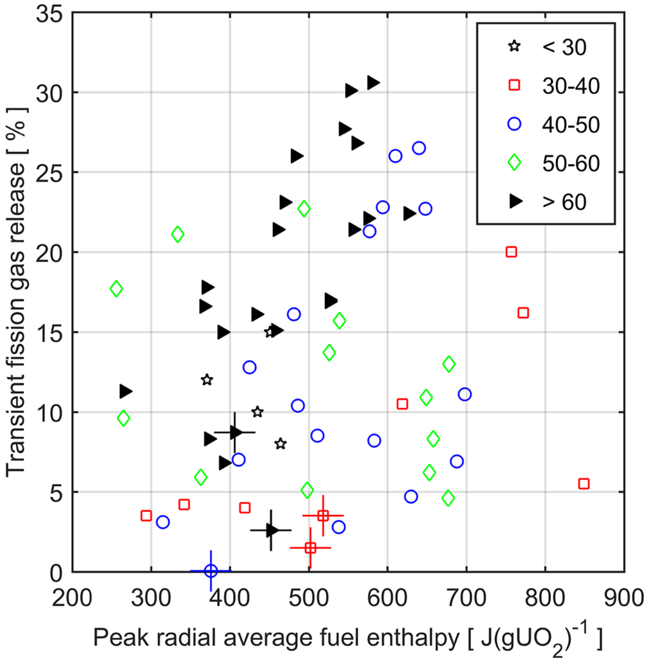

Fig. 16. Measured transient fission gas release for pre-irradiated UO_2 fuel rods, tested in the CABRI, NSRR and BIGR pulse reactor facilities, plotted versus peak radial average fuel enthalpy reached in each test [5]. The legend denotes fuel pellet burnup in $MWd(kgU)^{-1}$. Crosses indicate tests done on rods with large grain-size (25–40 μm) fuel pellets.

our model: for pellet average burnups <60 $MWd(kgU)^{-1}$, rupture of the narrow rim zone gives a negligible contribution to the calculated TFGR, since most of the released gas emanates from fractured grain faces in the non-restructured part of the pellet. Hence, burnup becomes less important below 60 $MWd(kgU)^{-1}$, and the fractional fission gas release is controlled by the size, number density and fission gas concentration of the grain face bubbles. These properties depend locally on the past histories of fuel temperature and fission rate, and hence, on the power history for the fuel rod.

The calculated results from our model also suggest a strong effect of local stress state on fuel pulverization and TFGR. For example, for the simulated LOCA tests in Section 3.2.2, most of the calculated pulverization and its associated fission gas release is triggered by the sudden drop of rod internal gas pressure that follows clad tube ballooning and burst. The rod depressurization, which is assumed to occur instantaneously in FRAPTRAN-QT-1.5, leads to immediate relaxation of the confining hydrostatic pressure in the fuel material. The calculated stress dependence, which is consistent with results from separate effect tests on TFGR and fuel fragmentation under controlled hydrostatic pressure conditions [29,118], is challenging from a modelling point of view: it is difficult to accurately calculate the pellet local stress state under transient conditions, since it is affected by pellet-cladding mechanical interaction, heterogeneous swelling, and effects of the radial temperature gradient on the thermal expansion of both the solid material and the gas enclosed in various cavities. Hence, the calculated fuel stresses depend on the applied model for PCMI, and more importantly, on the constitutive model applied for the fuel material, e.g. how fuel cracking, plasticity, creep and gaseous swelling are considered.

Since the FRAPCON and FRAPTRAN programmes used in our analyses do not calculate fuel stresses at all [40,41], we consider only the hydrostatic pressure in the fuel material and estimate this property through equations (23) and (24) for steady-state and transient conditions, respectively. The best-estimate value for the empirical parameter c_{th} in equation (24), as determined from our simulations of LOCA and RIA experiments, is 2×10^{-5} m. This value is comparable to the size of fine fuel fragments observed after pulverization tests on high burnup fuel [24,29]. The estimates of P_h defined by equations (23) and (24) give reasonable results when used in our models for fission gas behaviour. We note that for a radial temperature gradient of 1×10^6 Km^{-1}, typical for the outer part of the pellet during the early heat-up phase of a reactivity initiated accident, the last term in equation (24) reduces the local hydrostatic pressure by about 40 MPa. Our analyses in Sections 3.2.2 and 3.2.3 suggest that local fuel stresses induced by the radial temperature gradient are important for TFGR and fuel fragmentation for the studied RIA experiments, but less important for the considered LOCA tests, in which the radial temperature gradient is significantly milder. Yet, the radial temperature gradient would be much steeper in LOCA scenarios that are terminated by quenching of the overheated fuel, and it is reasonable to believe that fuel fragmentation caused by local thermal stresses would be more extensive in such scenarios.

Other investigators have tackled the problem of mechanical stress effects on fission gas behaviour differently. For example, Brankov et al. [140] and Khvostov [37] used $P_h = P_g^{gap}$ as an estimate for the fuel pellet hydrostatic pressure and added an auxiliary ‘trapping model’ for the fission gas, which restricted immediate gas release from vented grain boundaries and HBS pores in case the fuel had experienced PCMI. The degree of trapping was correlated to the time integral of the pellet-cladding contact pressure, whereby the effects of PCMI on fission gas release could be successfully captured.

Modelling of the fission gas behaviour could possibly benefit from advanced constitutive models for the fuel pellet material, by which the local stress state may be calculated with consideration of relevant deformation mechanisms, including cracking of the fuel material. Such constitutive models usually employ a smeared (continuum) representation of cracks in the material [141–144], since explicit (discrete) modelling of fuel pellet cracks is computationally demanding and still at the research front [145,146]. However, these state-of-the-art constitutive models tend to give very different results for the calculated stress distribution in the fuel pellet, even under stationary operating conditions, and it is therefore questionable if they would provide reliable boundary conditions for fission gas models.

As part of the model validation against experiments, we have estimated the local fracture energy of grain faces, $\mathscr{G}_{gb}$, and the local tensile strength of the HBS in the fuel pellet rim zone, σ_{hbs}^{cr}. As a first approximation, we have treated these local material properties as constants in the calculations and neglected any dependence on temperature or other parameters. The best-estimate value for $\mathscr{G}_{gb}$ is 4×10^{-3} Jm^{-2}, which is more than two orders of magnitude lower than the measured macroscopic (bulk) fracture energy of unirradiated polycrystalline UO_2 [147–149]. No measured data are available for the local fracture energy of grain boundaries, but molecular dynamics simulations indicate that it is comparable to that of bulk polycrystalline UO_2 in unirradiated conditions [150,151]. Hence, the very low fracture energy for the grain faces found in our analyses suggests that the grain faces would be significantly weakened by irradiation effects. They are obviously weakened by nucleation and growth of the gas bubbles that we consider in our model, but the precipitation of solid or liquid fission products may also lower their fracture energy.

The best-estimate value for the local tensile strength of the HBS, σ_{hbs}^{cr}, is 21 MPa. This is about 30 % of the bulk tensile strength reported for unirradiated UO_2 at room temperature [147,152–155]. The difference is partly related to the fact that σ_{hbs}^{cr} in our rupture criterion is applied without consideration of stress concentration effects of the spherical pores in the HBS. More precisely, equation (22) compares the *average* tensile stress across the ligament between neighbouring HBS pores with σ_{hbs}^{cr}, although the true tensile stress close to the pores will be significantly higher [81].

In conclusion, our validation shows that it is difficult to relate the local strength properties $\mathscr{G}_{gb}$ and σ_{hbs}^{cr} to the corresponding bulk properties of unirradiated UO_2, for which experimental data are available. The local properties have to be treated as model parameters that must be determined by calibration against suitable experiments. In addition to integral type tests as those presented in Sections 3.2.2 and 3.2.3, out-of-reactor fuel annealing tests under well controlled temperature and pressure conditions are useful sources of information. Such tests could possibly provide information on the temperature dependence of the local strength parameters.

4.2 Identified deficiencies of the models

The models presented in Section 2.2 tend to underestimate fission gas release by rupture of grain boundaries in the non-restructured part of the fuel pellet material. The main reason is that the simplified geometrical representation of the grain face cavities, i.e. a population of equal-size and equal-shape lenticular bubbles with a semi-dihedral angle of 47°, leads to underestimation of the cavity volume and intergranular fission gas content. As mentioned in Section 2.2.1, these lenticular bubbles have a lower ratio between bubble volume and projected area than the vermicular and multi-lobal bubbles that occupy real grain faces close to saturation [62]. Moreover, our models neglect the fission gas that is accumulated in large as-fabricated pores in the fuel material. It is reasonable to believe that this porosity, which typically amounts to 3-4 % of the pellet volume, contains a non-negligible fraction of the fuel fission gas inventory, and that this gas will be released in conjunction with grain boundary rupture [19,22]. One can also speculate that overpressurization of these large (>1 μm) pores will change the stress state in the nearby material, which could possibly contribute to grain boundary rupture. According to our models, the grain boundary fission gas inventory in the non-restructured material is typically no more than 5–10 % of the locally produced gas. This calculated fraction is lower than the total intergranular gas content reported from measurements on high burnup UO_2 fuel [156,157], which includes also the gas in large as-fabricated pores.

A simple way to compensate for this modelling deficiency is to increase the calculated grain boundary fission gas inventory by increasing the semi-dihedral angle, θ. As mentioned in Section 2.2.1, θ can be viewed as a tuning parameter that controls the ratio between volume and projected area of the grain face bubbles. Another approach would be to explicitly consider large as-fabricated pores as a specific cavity type in our models, in addition to grain face bubbles and HBS pores. This would represent the fuel microstructure with higher fidelity, at the expense of increased model complexity.

Moreover, the models do not perform well for overpower transients with time scales long enough for intragranular gas diffusion to take place. The models generally underestimate the transient fission gas release for such cases. The main reason is that the governing equations for intragranular diffusion are simplified by using a single equation with an effective fission gas diffusivity D_{eff} that considers trapping and resolution of gas in intragranular bubbles; see Section 2.1.1. This approach works well for steady-state operating conditions and for transients with insignificant intragranular gas diffusion, such as design basis LOCAs and RIAs. However, it is less useful for conditions where rapid changes in fuel temperature and fission rate are combined with sufficient hold times for considerable intragranular gas diffusion [158]. This is the case e.g. for power ramp tests with a typical duration of minutes to hours.

Changes in the cavity gas pressure are in the models calculated without consideration of possible volatilization of non-gaseous fission products. This is a poorly known phenomenon, but it has been speculated that volatilization of some fission products, notably Cs, could add to the cavity pressure increase during temperature excursions [33]. If it exists, the effect would be most likely in the pellet periphery, which is significantly heated above the normal steady-state operating temperature.

It should also be noticed that our models do not consider the possibility of cascade effects relating to rupture of grain face bubbles or HBS pores. Hence, the models neglect the possibility that elastic energy that is released from the gas and solid when a bubble or pore breaks could contribute to the rupture of nearby bubbles or pores, by analogy with fragmentation of tempered glass or other brittle materials with internal stresses [159].

4.3 Future work

Although the models proposed in Section 2 give reasonable results for fuel fine fragmentation and transient fission gas release in both LOCA and RIA conditions, further validation and calibration of the models against out-of-reactor separate effect tests as well as integral type LOCA and RIA tests are needed to firmly establish key model parameters. In addition to the local strength parameters $\mathscr{G}_{gb}$ and σ_{hbs}^{cr}, the semi-dihedral angle θ, the relaxation times τ_i for different modes of grain boundary gas release, and the vacancy diffusivity in UO_2 grain boundaries, D_{gb}^v, should be addressed in future calibration efforts. The relaxation times currently used in the model are first approximations, based on existing models for grain boundary fission gas release in steady-state [70] and RIA conditions [37], and have not been specifically calibrated against experimental data in our work. With regard to the grain boundary vacancy diffusivity, there are currently no low temperature data for D_{gb}^v. Such data are important, since our calculations indicate that the grain boundary vacancy diffusivity at low temperature has a strong effect on the evolution of grain face bubbles in the outer part of the fuel pellet. Further calibration should be done first and foremost against tests on fuel with a pellet average burnup of 60–70 MWd(kgU)$^{-1}$, since both experiments and our simulations of various LOCA scenarios suggest a transition from moderate to more extensive fuel fragmentation in this burnup range. Priority should also be given to tests, for which the operating life of the tested fuel is well known and documented. This is essential, in order to reduce uncertainties in the calculated pre-test conditions, e.g. fission gas distribution and fuel microstructure.

In the submodel for venting of fission gas by growth and interconnection of grain face bubbles, it is assumed that the bubble average size and number density remain unchanged as long as the bubble fractional area coverage is at the saturation threshold and fission gas is released; see Section 2.2.2. The status quo is achieved by equating the bubble gas pressure to the mechanical equilibrium pressure, a condition that serves as a basis for calculating the amount of local gas release. This modelling approach implies an upper limit for the average bubble size and a lower limit for the bubble number density, defined in Figure 2 by the transition from a solid to a dashed line style. From the data included in Figure 2, it is clear that the bubble population may evolve beyond these limits by disappearance of vented bubbles and growth of others. Hence, a more realistic modelling approach would be to allow continued growth and coarsening of grain face bubbles after onset of fission gas release, e.g. as in [65].

Moreover, it is assumed in our model that 20 % of the intragranular gas that is depleted during high burnup restructuring of the fuel material is released to the rod free volume. As noted in Section 2.3.1, this assumption is made in order to reproduce fission gas release data from fuel rods with moderately high burnup that have been irradiated in commercial LWRs, although there is no direct evidence of significant gas release connected with the restructuring per se. In fact, some data suggest that the enhanced gas release observed for high burnup LWR fuel rods would emanate from material subjacent to the restructured rim zone, and hypotheses for this release exist [48]. Our modelling of fission gas release as a direct consequence of HBS formation may need to be reconsidered, if convincing evidence for these release mechanisms appears.

The models presented in this paper were developed with the aim to support ongoing experimental studies on fuel rod behaviour in LOCA and RIA conditions. As shown in Sections 3.2.2 and 3.2.3, they can be used as tools for interpreting the results of such experiments, but they can also be used for planning and design of new experiments, in that influential parameters and testing conditions of particular interest can be identified by pre-test parametric studies. Both experiments and our computational analyses suggest that fuel burnup is a very important parameter for fuel fine fragmentation and TFGR in fuel with a pellet average burnup beyond 60 MWd(kgU)$^{-1}$. In this high burnup range, fragmentation of the HBS dominates the picture, and we do not expect that fuel fragmentation and fission gas release are much affected by the past power history of the fuel. The reason is that the HBS formation and the subsequent evolution of the fuel pellet rim zone are fairly insensitive to the power level; see Section 2.3.1. Empirical correlations with only local burnup and peak fuel temperature as input parameters, such as in [29], are probably adequate to discern whether significant fuel fine fragmentation will occur in this burnup range. However, the situation may be much different for fuel with lower burnup, in which the narrow rim zone gives a negligible contribution to the fuel fragmentation. In this case, we believe that the operating history of the fuel may be much more important to the extent of fuel fragmentation and TFGR under an accident, since it has a strong effect on the microstructure and fission gas distribution in the non-restructured fuel pellet material. This hypothesis should be investigated by parametric studies.

The effects of fuel pellet as-fabricated grain size on fuel fine fragmentation and TFGR in LOCA and RIA conditions are also worth studying with computational models. Modern LWR fuel designs often employ large grain UO_2 pellets with alleged superior thermal-mechanical performance under normal operation and anticipated operational occurrences [160,161]. The large grains are obtained either by use of additives (dopants) to the UO_2, or by modified process parameters (sintering time and temperature). Available data from RIA simulation tests show that transient fission gas release is lower for test rods with large grain (25–40 μm) UO_2 fuel than for rods with normal grain size (10–13 μm) fuel; see Figure 16. There are two possible explanations to the lower TFGR for large grain fuel: The fraction of intergranular gas is lower until fuel restructuring occurs, and the restructuring is delayed; see Section 2.3.1 and [91]. These two mechanisms could be investigated by modelling. In addition, it would be interesting to study the possible effects of fuel grain size on fuel fine fragmentation and TFGR in LOCA conditions, since experimental data from LOCA tests on large grain UO_2 fuel are currently unavailable.

The heating rate of the fuel during the accident is known to be important for fuel fine fragmentation and transient fission gas release. For example, Koo et al. evaluated data from 42 RIA simulation tests with the aim to identify the most influential parameters for TFGR by use of an artificial neural network [162]. They concluded that pellet average burnup was the most important parameter, followed by the ratio of peak fuel pellet enthalpy to power pulse width. This ratio is a measure of the fuel power density and heating rate [162]. In our models, the fuel heating rate affects the transient response of the fuel in several ways: It influences the local stress state through the magnitude of the radial temperature gradient, and it also controls to what extent the gas overpressure in grain face bubbles and HBS pores will have time to relax by bubble/pore growth or tortuous gas flow along grain boundary microcracks. We note that the stress effect may be important for fuel fine fragmentation and TFGR also under rapid cooling conditions, e.g. under quenching of the overheated fuel in the reflood phase of a LOCA. Early studies on unirradiated UO_2 fuel show that the thermal shock experienced by the fuel under quenching may lead to formation of microcracks [8]. The response of high burnup fuel to quenching is currently unclear, although a series of six LOCA simulation tests on high burnup fuel, where four of the tests were terminated by quenching and the other two by slow cool-down, has been reported [163]. Unfortunately, the fuel burnup and/or peak temperature in these tests were such that comparisons between the two groups of tests are inconclusive [163]. Our computational models could be used for exploring under what conditions quenching may have an effect on fuel fine fragmentation and gas release.

Finally, our models should be applied in best-estimate analyses of postulated design basis LWR LOCA and RIA scenarios. Computational models are essential for transferring the results of laboratory scale tests and experiments to conditions expected in commercial power reactors. This applies in particular to reactivity initiated accidents, where much of the experimental database originates from tests done under non-prototypical conditions [5].

This work was funded by the Swedish Radiation Safety Authority (SSM) under research contracts SSM 2015-4050 and SSM 2016-3944. Ali R. Massih is gratefully acknowledged for helpful comments on the manuscript.

Appendix A: Numerical solution to the bubble growth/shrinkage equations

Growth and shrinkage of grain face bubbles are in our model calculated through the Speight-Beeré model in equation (13), combined with White's relation between bubble size and number density in equation (12) and the Carnahan-Starling equation of state for the bubble gas. From the Speight-Beeré equation, the rate of change for the bubble volume can be written

$$\frac{dV_b}{dt} = G(t)F(t, V_b), \tag{A.1}$$

where $G(t) = 2\pi\Omega\omega D^v_{gb}(T(t))/k_BT(t)$ is independent of the bubble volume, whereas

$$F(t, V_b) = P_{ex}(t, V_b)/L(\phi_2(V_b)) \tag{A.2}$$

is an intricate function of V_b and time. P_{ex} is the bubble overpressure, defined through equation (1). At high temperature, the factor G turns large and the bubbles grow rapidly, such that P_{ex} tends to zero and equation (A.1) becomes stiff. For this reason, the numerical solution to equation (A.1) requires special methods. Standard solution schemes for ordinary differential equations, such as explicit Runge-Kutta algorithms, are unusable due to the short time steps required to ensure numerical stability of the solution. To overcome this problem, we consider implicit time integration of equation (A.1) from time t_o to $t_n = t_o + \Delta t$ in one step, viz.

$$\frac{\Delta V_b}{\Delta t} = G(t_n)F(t_n, V^o_b + \Delta V_b), \tag{A.3}$$

where V^o_b is the known bubble volume at time t_o and ΔV_b is the sought volume increment during the time step. We may approximate the end-of-timestep value of F by a Taylor series expansion in V_b, which inserted into equation (A.3) leads to

$$\Delta V_b \approx \Delta t F(t_n, V^o_b)\left(\frac{1}{G(t_n)} - \Delta t\frac{\partial F}{\partial V_b}\right)^{-1}. \tag{A.4}$$

The partial derivative of F in equation (A.4) should be evaluated for $V_b = V^o_b$ and $t = t_n$, i.e. the end-of-timestep values for all variables except V_b should be used in its evaluation. Considering a lenticular bubble with projected radius r_b as shown in Figure 1, it follows from equations (1) and (A.2) that

$$\frac{\partial F}{\partial V_b} = \frac{1}{L}\frac{\partial r_b}{\partial V_b}\left(\frac{\partial P_g}{\partial r_b} - \frac{\partial P_s}{\partial r_b} - \frac{P_{ex}}{L}\frac{\partial L}{\partial \phi_2}\frac{\partial \phi_2}{\partial r_b}\right). \tag{A.5}$$

From equations (1), (12), (14)–(16), we find

$$\frac{\partial r_b}{\partial V_b} = \frac{r_b}{3V_b} = \frac{1}{4\pi\tilde{\eta}r_b^2}, \tag{A.6}$$

$$\frac{\partial P_s}{\partial r_b} = -\frac{P_s}{r_b} = -\frac{2\gamma\sin\theta}{r_b^2}, \tag{A.7}$$

$$\frac{\partial L}{\partial \phi_2}\frac{\partial \phi_2}{\partial r_b} = \frac{1}{r_b}\left(2\phi_2^3 - 5\phi_2^2 + 4\phi_2 - 1\right). \tag{A.8}$$

The gas pressure in small, newly nucleated grain face bubbles may reach values that are outside the range of validity of simple equations of state, such as the ideal gas law or van der Waals equation [164]. For this reason, the bubble gas pressure is in our model calculated from local temperature and gas atom density through the Carnahan-Starling equation of state [76]

$$P_g = \frac{6k_BT}{\pi d^3}\frac{(y + y^2 + y^3 - y^4)}{(1 - y)^3}. \tag{A.9}$$

Here, $y = (\pi d^3/6)(N/V_b)$, where N/V_b is the gas atom density in the bubble and d is the diameter of a hard sphere that represents the gas atom. More precisely, we make use of the results for Xe, calculated with the

Lennard-Jones potential by Brearley and MacInnes [165]

$$d = \sigma_e(0.9937 - 0.041168 \ln(k_B T/\epsilon_e)), \tag{A.10}$$

where $\sigma_e = 4.032 \times 10^{-10}$ m and $\epsilon_e/k_B = 219$ K. The gas atom density in the grain face bubbles is calculated from the surface concentration of gas atoms at the grain boundaries, N_{gb}, see Section 2.1.2, and the number density of bubbles, n_b

$$\frac{N}{V_b} = \frac{N_{gb}}{n_b V_b} = \frac{3N_{gb}}{4\tilde{\eta}\phi_2 r_b}. \tag{A.11}$$

By using equation (A.11) in the expression for y in equation (A.9) and noting that ϕ_2 depends on r_b through equation (15), we arrive at

$$\begin{aligned}\frac{\partial P_g}{\partial r_b} &= \frac{\partial P_g}{\partial y}\frac{\partial y}{\partial r_b}\\ &= -\frac{P_g(3-4\phi_2)(1+4y+4y^2-4y^3+y^4)}{r_b(1-2y^3+y^4)}.\end{aligned} \tag{A.12}$$

Hence, all the partial derivatives entering the right-hand-side of equation (A.5) can be analytically calculated through equations (A.6)–(A.12), and the incremental change in volume during the time step can then be calculated through equation (A.4). In our numerical implementation, the time step Δt is adaptively set, such that the relative change in bubble volume ($\Delta V_b/V_b^o$) is <0.01 in any time step.

References

1. G.P. Mezzi, Nucl. Eng. Des. **73**, 83 (1983)
2. M. Oguma, Nucl. Eng. Des. **76**, 35 (1983)
3. L.A. Walton, D.L. Husser, in *Water Reactor Fuel Element Performance Computer Modelling*, edited by J.H. Gittus (Applied Science Publishers, London, UK, 1983), Chap. 7, pp. 115–135
4. O. Coindreau, F. Fichot, J. Fleurot, Nucl. Eng. Des. **255**, 68 (2013)
5. Nuclear fuel behaviour under reactivity-initiated accident (RIA) conditions. Report 6847, OECD Nuclear Energy Agency, Paris, France, 2010
6. D. Lespiaux, J. Noirot, P. Menut, in *1997 International Topical Meeting on Light Water Reactor Fuel Performance* (American Nuclear Society, Portland, OR, 1997), pp. 650–658
7. T. Fuketa, T. Nakmura, H. Sasajima, F. Nagase, H. Uetsuka, K. Kikuchi, T. Abe, in *2000 International Topical Meeting on Light Water Reactor Fuel Performance* (American Nuclear Society, Park City, UT, USA, 2000), pp. 359–374
8. M. Oguma, J. Nucl. Mater. **127**, 67 (1985)
9. O.D. Slagle, C.A. Hinman, E.T. Weber, Experiments on melting and gas release behavior of irradiated fuel. Tech. Rep. HEDL-TME 74-17, Hanford Engineering Development Laboratory, Richland, WA, USA, 1974
10. L.W. Deitrich, J.F. Jackson, in *IAEA-IWGFR specialist's meeting on role of fission products in whole core accidents*, vol. IWGFR–19 (International Atomic Energy Agency, AERE, Harwell, UK, 1977), Vol. IWGFR–19, pp. 66–87
11. R.J. DiMelfi, J.M. Kramer, Nucl. Technol. **62**, 51 (1983)
12. S.A. Wright, E.A. Fischer, Eur. Appl. Res. Rep. Nucl. Sci. Technol. **5**, 1393 (1984)
13. J.R. Matthews, A.H. Harker, D.S. Whitmell, in *International conference on radiation materials science* (Kharkov Fiziko-Tekhnicheskij Institut, Alushta, Soviet Union, 1990), Vol. 1, pp. 184–214
14. E.E. Gruber, W.R. Bohl, M.G. Stevenson, in *Reactor development program progress report* (Argonne National Laboratory, Argonne, IL, USA, 1973), ANL-RDP-15, Chap. 9.1
15. M.W. Finnis, (report unavailable). Harwell Research Report AERE-R 8537, Atomic Energy Research Establishment, Harwell, Oxon, UK, 1976
16. R.J. DiMelfi, L.W. Deitrich, Nucl. Technol. **43**, 328 (1979)
17. D.H. Worledge, Fuel fragmentation by fission gases during rapid heating. Tech. Rep. SAND80-0328 (NUREG/CR-1611), Sandia National Laboratories, Albuquerque, NM, USA (1980)
18. S.M. Gehl, Release of fission gas during transient heating of LWR fuel. Tech. Rep. ANL-80-108, Argonne National Laboratory, Lemont, IL, USA (1982). Also as U.S. NRC report NUREG/CR-2777
19. F. Lemoine, J. Nucl. Mater. **248**, 238 (1997)
20. T. Fuketa, H. Sasajima, Y. Mori, K. Ishijima, J. Nucl. Mater. **248**, 249 (1997)
21. V.V. Likhanskii, L.V. Matveev, Atom. Energy **87**, 490 (1999)
22. F. Lemoine, J. Papin, J.M. Frizonnet, B. Cazalis, H. Rigat, in *Fission Gas Behaviour in Water Reactor Fuels – Seminar Proceedings* (OECD Nuclear Energy Agency, Cadarache, France, 2000), pp. 175–187
23. K. Une, S. Kashibe, A. Takagi, J. Nucl. Sci. Technol. **43**, 1161 (2006)
24. J.P. Hiernaut, T. Wiss, J.Y. Colle, H. Thiele, C.T. Walker, W. Goll, R.J.M. Konings, J. Nucl. Mater. **377**, 313 (2008)
25. A. Puranen, M. Granfors, P. Askeljung, D. Jädernäs, M. Flanagan, in *Proceedings of 2013 LWR Fuel Performance/TopFuel/WRFPM* (American Nuclear Society, Charlotte, NC, USA, 2013), pp. 669–674
26. B.C. Oberländer, W. Wiesenack, Overview of Halden reactor LOCA experiments (with emphasis on fuel fragmentation) and plans. Report IFE/KR/E-2014/001, Institute for Energy Technology, Kjeller, Norway, 2014
27. NEA Studsvik cladding integrity project (SCIP-III). https://www.oecd-nea.org/jointproj/scip-3.html (2019)
28. S. Yagnik, J.A. Turnbull, J. Noirot, C.T. Walker, L. Hallstadius, N. Waeckel, P. Blanpain, in *2014 Water Reactor Fuel Performance Meeting (WRFPM-2014)* (Atomic Energy Society of Japan, Sendai, Japan, 2014)
29. J.A. Turnbull, S.K. Yagnik, M. Hirai, D.M. Staicu, C.T. Walker, Nucl. Sci. Eng. **179**, 477 (2015)
30. A. Bianco, Experimental investigation on the causes for pellet fragmentation under LOCA conditions. Ph.D. thesis, Technischen Universität München, Germany, 2015
31. A. Bianco, C. Vitanza, M. Seidl, A. Wensauer, W. Faber, R. Marcian-Juan, J. Nucl. Mater. **465**, 260 (2015)
32. Nuclear fuel behaviour in loss-of-coolant accident (LOCA) conditions. Report 6846, OECD Nuclear Energy Agency, Paris, France, 2009

33. Report on fuel fragmentation, relocation and dispersal. Report NEA/CSNI/R(2016)16, OECD Nuclear Energy Agency, Paris, France, 2016
34. K. Kulacsy, J. Nucl. Mater. **466**, 409 (2015)
35. M. Suzuki, Y. Udagawa, T. Sugiyama, F. Nagase, in *Proceedings of TopFuel 2012* (European Nuclear Society, Manchester, UK, 2012), pp. 554–559
36. A. Moal, V. Georgenthum, O. Marchand, Nucl. Eng. Des. **280**, 150 (2014)
37. G. Khvostov, Nucl. Eng. Des. **328**, 36 (2018)
38. I. Guenot-Delahaie, J. Sercombe, T. Helfer, P. Goldbronn, E. Federici, T.L. Jolu, A. Parrot, C. Delafoy, C. Bernaudat, Nucl. Eng. Technol. **50**, 268 (2018)
39. M. Tonks, D. Andersson, R. Devanathan, R. Dubourg, A. El-Azab, M. Freyss, F. Iglesias, K. Kulacsy, G. Pastore, S.R. Phillpot, M. Welland, J. Nucl. Mater. **504**, 300 (2018)
40. K.J. Geelhood, W.G. Luscher, P.A. Raynaud, I.E. Porter, FRAPCON-4.0: A computer code for the calculation of steady-state, thermal-mechanical behavior of oxide fuel rods for high burnup. Report PNNL-19418, Vol. 1, Rev. 2, Pacific Northwest National Laboratory, Richland, WA, USA, 2015
41. K.J. Geelhood, W.G. Luscher, J.M. Cuta, FRAPTRAN-1.5: A computer code for the transient analysis of oxide fuel rods. Report PNNL-19400, Vol. 1, Rev. 1, Pacific Northwest National Laboratory, Richland, WA, USA, 2014
42. L.O. Jernkvist, A. Massih, in *Fuel Modelling in Accident Conditions (FUMAC): Country Reports from Participants* (International Atomic Energy Agency, Vienna, Austria, 2019), IAEA-TECDOC, Vol. 2
43. E.N. Hodkin, J. Nucl. Mater. **88**, 7 (1980)
44. R.O.A. Hall, M.J. Mortimer, D.A. Mortimer, J. Nucl. Mater. **148**, 237 (1987)
45. M.V. Speight, Nucl. Sci. Eng. **37**, 180 (1969)
46. K. Forsberg, A.R. Massih, J. Nucl. Mater. **135**, 140 (1985)
47. P. Hermansson, A.R. Massih, J. Nucl. Mater. **304**, 204 (2002)
48. J. Rest, M.W.D. Cooper, J. Spino, J.A. Turnbull, P. van Uffelen, C.T. Walker, J. Nucl. Mater. **513**, 310 (2019)
49. J.A. Turnbull, C.A. Friskney, J.R. Findlay, F.A. Johnson, A.J. Walter, J. Nucl. Mater. **107**, 168 (1982)
50. J.A. Turnbull, R.J. White, C. Wise, in *Water reactor fuel element computer modelling in steady state, transient and accident conditions* (International Atomic Energy Agency, Vienna, Austria, 1988), IAEA-TC-659/3.5, pp. 174–181
51. F.S. Ham, J. Phys. Chem. Solids **6**, 335 (1958)
52. R.J. White, M.O. Tucker, J. Nucl. Mater. **118**, 1 (1983)
53. H. Matzke, Radiat. Effects **53**, 219 (1980)
54. C. Baker, J. Nucl. Mater. **66**, 283 (1977)
55. T.S. Noggle, J.O. Stiegler, J. Appl. Phys. **31**, 2199 (1960)
56. D.R. Olander, *Fundamental Aspects of Nuclear Reactor Fuel Elements* (National Technology Information Services, Springfield, VA, USA, 1976)
57. B.J. Lewis, J. Nucl. Mater. **148**, 28 (1987)
58. I.J. Hastings, J. Nucl. Mater. **54**, 138 (1974)
59. C.T. Walker, P. Knappik, M. Mogensen, J. Nucl. Mater. **160**, 10 (1988)
60. G.J. Small, in *Water Reactor Fuel Element Computer Modelling in Steady State, Transient and Accident Conditions* (IAEA, Vienna, Austria, 1989), IWGFPT/32, pp. 209–220
61. S. Kashibe, K. Une, J. Nucl. Sci. Technol. **28**, 1090 (1991)
62. R.J. White, J. Nucl. Mater. **325**, 61 (2004)
63. R.J. White, R.C. Corcoran, P.J. Barnes, NEA-1705 IFPE/CAGR-UOX-SWELL: Fuel swelling data obtained from the AGR/Halden ramp test program. OECD Nuclear Energy Agency, Paris, France, 2006
64. M.S. Veshchunov, J. Nucl. Mater. **374**, 44 (2008)
65. G. Pastore, L. Luzzi, V.D. Marcello, P. van Uffelen, Nucl. Eng. Des. **256**, 75 (2013)
66. D. Hull, D.E. Rimmer, Philos. Mag. **4**, 673 (1959)
67. R. Raj, M.F. Ashby, Acta Metall. **23**, 653 (1975)
68. M.V. Speight, W. Beeré, Metal Sci. **9**, 190 (1975)
69. G.I. Reynolds, W.B. Beeré, P.T. Sawbridge, J. Nucl. Mater. **41**, 112 (1971)
70. T. Kogai, J. Nucl. Mater. **244**, 131 (1997)
71. E.E. Gruber, J. Nucl. Mater. **110**, 223 (1982)
72. M.R. Hayns, M.W. Finnis, Eur. Appl. Res. Rep. Nucl. Sci. Technol. **1**, 255 (1979)
73. J.R. Matthews, M.H. Wood, J. Nucl. Mater. **91**, 241 (1980)
74. T. Kogai, K. Ito, Y. Iwano, J. Nucl. Mater. **158**, 64 (1988)
75. P. van Uffelen, in *2000 International Topical Meeting on Light Water Reactor Fuel Performance* (American Nuclear Society, Park City, UT, USA, 2000), pp. 356–368
76. N.F. Carnahan, K.E. Starling, J. Chem. Phys. **51**, 635 (1969)
77. P.C. Millett, Comp. Mater. Sci. **53**, 31 (2012)
78. D. Sabogal-Suarez, J.D. Alzate-Cardona, E. Restrepo-Parra, J. Nucl. Mater. **475**, 81 (2016)
79. P. van Uffelen, Contribution to the modelling of fission gas release in light water reactor fuel. Thesis BLG-907, Université de Liège, Belgium, 2002
80. T. Kogai, Y. Iwano, J. Nucl. Sci. Technol. **27**, 1017 (1990)
81. L.O. Jernkvist, To appear in Prog. Nucl. Energy
82. P. Chakraborty, M.R. Tonks, G. Pastore, J. Nucl. Mater. **452**, 95 (2014)
83. T.L. Anderson, *Fracture mechanics: Fundamentals and applications*, 3rd edn. (CRC Press, Boca Raton, FL, USA, 2005)
84. D. Baron, M. Kinoshita, P. Thevenin, R. Largenton, Nucl. Eng. Technol. **41**, 199 (2009)
85. V.V. Rondinella, T. Wiss, Mater. Today **13**, 24 (2010)
86. T. Wiss, V.V. Rondinella, R.J.M. Konings, D. Staicu, D. Papaioannou, S. Bremier, P. Pöml, O. Benes, J.Y. Colle, P. van Uffelen, A. Schubert, F. Cappia, M. Marchetti, D. Pizzocri, F. Jatuff, W. Goll, T. Sonoda, A. Sasahara, S. Kitajima, M. Kinoshita, Radiochim. Acta **105**, 893 (2017)
87. C.T. Walker, J. Nucl. Mater. **275**, 56 (1999)
88. K. Nogita, K. Une, M. Hirai, K. Ito, K. Ito, Y. Shirai, J. Nucl. Mater. **248**, 196 (1997)
89. K. Une, M. Hirai, K. Nogita, T. Hosokawa, Y. Suzawa, S. Shimizu, Y. Etoh, J. Nucl. Mater. **278**, 54 (2000)
90. Y. Tsukuda, Y. Kosaka, T. Kido, S. Doi, T. Sendo, P. Gonzales, J.M. Alonso, in *ENS TopFuel 2003* (European Nuclear Society, Wurzburg, Germany, 2003)
91. J. Noirot, Y. Pontillon, S. Yagnik, J.A. Turnbull, J. Nucl. Mater. **462**, 77 (2015)
92. M. Mogensen, J.H. Pearce, C.T. Walker, J. Nucl. Mater. **264**, 99 (1999)
93. J. Noirot, L. Desgranges, J. Lamontagne, J. Nucl. Mater. **372**, 318 (2008)
94. J. Noirot, I. Aubrun, L. Desgranges, K. Hanifi, J. Lamontagne, B. Pasquet, C. Valot, P. Blanpain, H. Cognon, Nucl. Eng. Technol. **41**, 155 (2009)

95. J. Noirot, Y. Pontillon, S. Yagnik, J.A. Turnbull, T. Tverberg, J. Nucl. Mater. **446**, 163 (2014)
96. J. Spino, D. Papaioannou, J.P. Glatz, J. Nucl. Mater. **328**, 67 (2004)
97. J. Spino, A.D. Stalios, H.S. Cruz, D. Baron, J. Nucl. Mater. **354**, 66 (2006)
98. R. Restani, M. Horvath, W. Goll, J. Bertsch, D. Gavillet, A. Hermann, M. Martin, C.T. Walker, J. Nucl. Mater. **481**, 88 (2016)
99. K. Une, K. Nogita, Y. Suzawa, K. Hayashi, K. Ito, Y. Etoh, in *2000 International Topical Meeting on Light Water Reactor Fuel Performance* (American Nuclear Society, Park City, UT, USA, 2000), pp. 775–785
100. K. Une, K. Nogita, T. Shiratori, K. Hayashi, J. Nucl. Mater. **288**, 20 (2001)
101. L.O. Jernkvist, A.R. Massih, Models for fuel rod behaviour at high burnup. Report 2005:41, Swedish Nuclear Power Inspectorate (SKI), Stockholm, Sweden, 2004. Available at: www.ssm.se
102. J. Rest, J. Nucl. Mater. **326**, 175 (2004)
103. L. Holt, A. Schubert, P. van Uffelen, C.T. Walker, E. Fridman, T. Sonoda, J. Nucl. Mater. **452**, 166 (2014)
104. M. Kinoshita, T. Sonoda, S. Kitajima, A. Sasahara, T. Kameyama, T. Matsumura, E. Kolstad, V.V. Rondinella, C. Ronchi, J.P. Hiernaut, T. Wiss, F. Kinnart, J. Ejton, D. Papaioannou, H. Matzke, in *2004 International Meeting on LWR Fuel Performance* (American Nuclear Society, Orlando, FL, USA, 2004), pp. 207–213
105. G. Khvostov, K. Mikityuk, M.A. Zimmermann, Nucl. Eng. Des. **241**, 2983 (2011)
106. C.T. Walker, S. Bremier, S. Portier, R. Hasnaoui, W. Goll, J. Nucl. Mater. **393**, 212 (2009)
107. L. Gao, B. Chen, Z. Xiao, S. Jiang, J. Yu, Nucl. Eng. Des. **260**, 11 (2013)
108. J. Spino, J. Rest, W. Goll, C.T. Walker, J. Nucl. Mater. **346**, 131 (2005)
109. F. Cappia, D. Pizzocri, A. Schubert, P. van Uffelen, G. Paperini, D. Pellottiero, R. Macian-Juan, V.V. Rondinella, J. Nucl. Mater. **480**, 138 (2016)
110. H.X. Xiao, C.S. Long, Nucl. Eng. Techn. **48**, 1002 (2016)
111. K. Lassmann, C.T. Walker, J. van de Laar, F. Lindström, J. Nucl. Mater. **226**, 1 (1995)
112. F. Lemoine, D. Baron, P. Blanpain, in *Proceedings of 2010 LWR Fuel Performance/TopFuel/WRFPM* (American Nuclear Society, Orlando, FL, USA, 2010), pp. 539–551
113. P. Blair, A. Romano, C. Hellwig, R. Chawla, J. Nucl. Mater. **350**, 232 (2006)
114. D. Pizzocri, F. Cappia, L. Luzzi, G. Pastore, V.V. Rondinella, P. van Uffelen, J. Nucl. Mater. **487**, 23 (2017)
115. J.O. Barner, M.E. Cunningham, M.D. Freshley, D.D. Lanning, Nucl. Technol. **102**, 210 (1993)
116. L.C. Bernard, J.L. Jacoud, P. Vesco, J. Nucl. Mater. **302**, 125 (2002)
117. C.B. Lee, D.H. Kim, Y.M. Kim, Y.S. Yang, S.K. Kim, Y.H. Jung, Y.B. Chun, H.S. Seo, in *2004 International Meeting on LWR Fuel Performance* (American Nuclear Society, Orlando, FL, USA, 2004), pp. 200–206
118. K. Une, S. Kashibe, K. Hayashi, J. Nucl. Sci. Technol. **39**, 668 (2002)
119. A. Romano, M.I. Horvath, R. Restani, J. Nucl. Mater. **361**, 62 (2007)
120. P. Blair, Modelling of fission gas behaviour in high burnup nuclear fuel. Thesis no 4084, École polytechnique fédérale de Lausanne, Switzerland, 2008
121. M. Lemes, A. Soba, A. Denis, J. Nucl. Mater. **456**, 174 (2015)
122. Y.H. Koo, B.H. Lee, J.S. Cheon, D.S. Sohn, J. Nucl. Mater. **295**, 213 (2001)
123. G.W. Greenwood, A.J.E. Foreman, D.E. Rimmer, J. Nucl. Mater. **1**, 305 (1959)
124. K. Nogita, K. Une, J. Nucl. Mater. **226**, 302 (1995)
125. M.D. Rintoul, S. Torquato, J. Phys. A: Math. Gen. **30**, L585 (1997)
126. L.J. Siefken, E.W. Coryell, E.A. Harvego, J.K. Hohorst, SCDAP/RELAP5/MOD 3.3 code manual, MATPRO - A library of materials properties for light water reactor accident analysis. Report NUREG/CR-6150, Vol. 4, Rev. 2, U.S. Nuclear Regulatory Commission, Washington, DC, USA, 2001
127. G.T. Lawrence, J. Nucl. Mater. **71**, 195 (1978)
128. G.L. Reynolds, B. Burton, J. Nucl. Mater. **82**, 22 (1979)
129. K. Govers, S.E. Lemehov, M. Verwerft, J. Nucl. Mater. **405**, 252 (2010)
130. K. Govers, S.E. Lemehov, M. Verwerft, Defect Diffus. Forum **323–325**, 215 (2012)
131. M.R. Eslami, R.B. Hetnarski, J. Ignaczak, N. Noda, N. Sumi, Y. Tanigawa, in *Theory of elasticity and thermal stresses: explanations, problems and solutions*. Solid Mechanics and Its Applications (Springer, Dordrecht, Netherlands, 2013), Vol. 197
132. K.J. Geelhood, W.G. Luscher, FRAPCON-4.0: Integral assessment. Report PNNL-19418, Vol. 2, Rev. 2, Pacific Northwest National Laboratory, Richland, WA, USA, 2015
133. J. Karlsson, P. Beccau, P.M. et al., in *Proceedings of TopFuel 2018* (European Nuclear Society, Prague, Czech Republic, 2018)
134. M. Veshchunov, J. Stuckert, P. van Uffelen, W. Wiesenack, J. Zhang, in *Proceedings of TopFuel 2018* (European Nuclear Society, Prague, Czech Republic, 2018)
135. Fuel modelling in accident conditions (FUMAC): Final report of a coordinated research project CRP T12028 (2014−2018). Report IAEA-TECDOC, Vol. 1, International Atomic Energy Agency, Vienna, Austria, 2019
136. International fuel performance experiments (IFPE) database. OECD Nuclear Energy Agency, Paris, France, 2019
137. J. Papin, B. Cazalis, J.M. Frizonnet, J. Desquines, F. Lemoine, V. Georgenthum, F. Lamare, M. Petit, Nucl. Technol. **157**, 230 (2007)
138. M. Petit, O. Marchand, F. Barre, P. Giordano, in *Fuel behaviour and modelling under severe transient and loss of coolant accident (LOCA) conditions, Mito, Japan, Oct. 18-21, 2011* (International Atomic Energy Agency, Vienna, Austria, 2011), IAEA-TECDOC-CD-1709, pp. 25–42
139. Pressurized water reactor control rod ejection and boiling water reactor control rod drop accidents. Draft Regulatory Guide 1327, U.S. Nuclear Regulatory Commission, Washington, DC, USA, 2019
140. V. Brankov, G. Khvostov, K. Mikityuk, A. Pautz, R. Restani, S. Abolhassani, G. Ledergerber, W. Wiesenack, Nucl. Eng. Des. **305**, 559 (2016)
141. L.O. Jernkvist, Nucl. Eng. Des. **176**, 273 (1997)

142. V. Guicheret-Retel, F. Trivaudey, M.L. Boubakar, P. Thevenin, Nucl. Eng. Des. **232**, 249 (2004)
143. B. Michel, J. Sercombe, G. Thouvenin, R. Chatelet, Eng. Fract. Mech. **75**, 3581 (2008)
144. N. Marchal, C. Campos, C. Garnier, Comp. Mater. Sci. **45**, 821 (2009)
145. R.L. Williamson, D.A. Knoll, in *20th International Conference on Structural Mechanics in Reactor Technology (SMiRT-20)* (Espoo, Finland, 2009)
146. R. Mella, M.R. Wenman, J. Nucl. Mater. **467**, 58 (2015)
147. A.G. Evans, R.W. Davidge, J. Nucl. Mater. **33**, 249 (1969)
148. T.R.G. Kutty, K.N. Chandrasekharan, J.P. Panakkal, J.K. Ghosh, J. Mater. Sci. Lett. **6**, 260 (1987)
149. J.M. Gatt, J. Sercombe, I. Aubrun, J.C. Menard, Eng. Fail. Anal. **47**, 299 (2015)
150. P.V. Nerikar, K. Rudman, T.G. Desai, D. Byler, C. Unal, K.J. McClellan, S.R. Phillpot, S.B. Sinott, P. Peralta, B.P. Uberuaga, C.R. Stanek, J. Am. Ceram. Soc. **94**, 1893 (2011)
151. Y. Zhang, P.C. Millett, M.R. Tonks, X.M. Bai, S.B. Biner, J. Nucl. Mater. **452**, 296 (2014)
152. R.F. Canon, J.T.A. Roberts, R.J. Beals, J. Am. Ceram. Soc. **54**, 105 (1971)
153. J.T.A. Roberts, Y. Ueda, J. Am. Ceram. Soc. **55**, 117 (1972)
154. T. Tachibana, H. Furuya, M. Koizumi, J. Nucl. Sci. Technol. **16**, 266 (1979)
155. M. Oguma, J. Nucl. Sci. Technol. **19**, 1005 (1982)
156. S. Ravel, G. Eminet, E. Muller, L. Caillot, in *Fission Gas Behaviour in Water Reactor Fuels - Seminar Proceedings* (OECD Nuclear Energy Agency, Cadarache, France, 2000), pp. 347–356
157. Y. Pontillon, M.P. Ferroud-Plattet, D. Parrat, S. Ravel, G. Ducros, C. Struzik, I. Aubrun, G. Eminet, J. Lamontagne, J. Noirot, A. Harrer, in *2004 International Meeting on LWR Fuel Performance* (American Nuclear Society, Orlando, FL, USA, 2004), pp. 490–499
158. G. Pastore, D. Pizzocri, C. Rabiti, T. Barani, P. van Uffelen, L. Luzzi, J. Nucl. Mater. **509**, 687 (2018)
159. J.M. Barsom, J. Am. Ceram. Soc. **51**, 75 (1968)
160. J. Arborelius, K. Backman, L. Hallstadius, M. Limbäck, J. Nilsson, B. Rebensdorff, G. Zhou, K. Kitano, R. Löfström, G. Rönnberg, J. Nucl. Sci. Technol. **43**, 967 (2006)
161. C. Delafoy, P. Dewes, in *TopFuel 2006* (European Nuclear Society, Salamanca, Spain, 2006), pp. 487–491
162. Y.H. Koo, J.Y. Oh, B.H. Lee, Y.W. Tahk, K.W. Song, J. Nucl. Mater. **405**, 33 (2010)
163. M. Flanagan, P. Askeljung, A. Puranen, Post-test examination results from integral, high-burnup, fueled LOCA tests at Studsvik nuclear laboratory. Report NUREG-2160, U.S. Nuclear Regulatory Commission, Washington, DC, USA, 2013
164. H.X. Xiao, C.S. Long, Chin. Phys. B **23**, 020502 (2014)
165. I.R. Brearley, D.A. Macinnes, J. Nucl. Mater. **95**, 239 (1980)

Cite this article as: Lars O. Jernkvist, Modelling of fine fragmentation and fission gas release of UO_2 fuel in accident conditions, EPJ Nuclear Sci. Technol. **5**, 11 (2019)